

DP-NeRF: Deblurred Neural Radiance Field with Physical Scene Priors

Dogyoon Lee¹ Minhyeok Lee¹ Chajin Shin¹ Sangyoun Lee^{1,2}

¹Yonsei University

²Korea Institute of Science and Technology (KIST)

{nemotio, hydragon516, chajin, syleee}@yonsei.ac.kr

Abstract

Neural Radiance Field (NeRF) has exhibited outstanding three-dimensional (3D) reconstruction quality via the novel view synthesis from multi-view images and paired calibrated camera parameters. However, previous NeRF-based systems have been demonstrated under strictly controlled settings, with little attention paid to less ideal scenarios, including with the presence of noise such as exposure, illumination changes, and blur. In particular, though blur frequently occurs in real situations, NeRF that can handle blurred images has received little attention. The few studies that have investigated NeRF for blurred images have not considered geometric and appearance consistency in 3D space, which is one of the most important factors in 3D reconstruction. This leads to inconsistency and the degradation of the perceptual quality of the constructed scene. Hence, this paper proposes a DP-NeRF, a novel clean NeRF framework for blurred images, which is constrained with two physical priors. These priors are derived from the actual blurring process during image acquisition by the camera. DP-NeRF proposes rigid blurring kernel to impose 3D consistency utilizing the physical priors and adaptive weight proposal to refine the color composition error in consideration of the relationship between depth and blur. We present extensive experimental results for synthetic and real scenes with two types of blur: camera motion blur and defocus blur. The results demonstrate that DP-NeRF successfully improves the perceptual quality of the constructed NeRF ensuring 3D geometric and appearance consistency. We further demonstrate the effectiveness of our model with comprehensive ablation analysis. ^{1 2}

1. Introduction

The synthesis of the photo-realistic novel view image of complex three-dimensional (3D) scenes has advanced rapidly due to the emergence of the Neural Radiance Field (NeRF) [26]. NeRF has introduced implicit scene representation to the field, which maps an arbitrary continuous

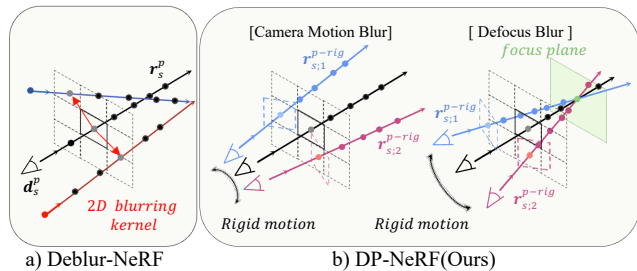


Figure 1. (a) Deblur-NeRF models blurring kernel based on 2D offset on the image pixels. This modeling breaks the consistency in trained neural radiance field due to the lack of a 3D consistency priors. However, (b) DP-NeRF can render clean neural radiance field guaranteeing the 3D consistency with rigid motion of the camera based on the physical priors of the blur occurrence.

3D coordinate to the volume density and radiance color using volume-rendering technique and implicit neural representation. NeRF densely reconstructs continuous 3D space to produce photorealistic rendered images with novel view.

Though NeRF has achieved remarkable success in a variety of fields, most of the NeRF variants have been designed and tested for a carefully controlled environment that requires well-captured images from multiple views with calibrated camera parameters. However, various forms of noises are usually included in the data captured for the NeRF in real scenarios, complicating geometric and appearance consistency in 3D representation.

Several NeRF variants have attempted to reconstruct 3D scene in the presence of noise, including exposure noise [8, 11, 25], motion [17–19, 29, 30, 33, 49, 55], illumination changes [6, 23, 57], and aliasing [1, 2]. However, although it frequently occurs in real-world settings, blur has not been sufficiently addressed to date, despite the fact that it generates critical artifacts in 3D scene reconstruction. Deblur-NeRF [22] introduced blurring kernel estimation for a NeRF by imitating in-camera blurred image acquisition based on a blind deblurring method. Their method demonstrated excellent performance and produced clearly rendered images from multi-view images. However, the blurring kernel in [22] is implemented by optimizing ray deformation and composition weights depending on the 2D

¹Code: <https://github.com/dogyoonlee/DP-NeRF>

²Project: <https://dogyoonlee.github.io/dpnerf/>

pixel location independently, leading to insufficient 3D information. In reality, the blurring process occurs simultaneously for all pixels in an image due to the physical process of in-camera image acquisition, but [22] overlooks the prior for blurring, leading to a lack of consistency in an image. Moreover, the designed kernel can be inherently optimized to suboptimal in regions with complex depth or similar appearance due to the independent optimization of the deformation of each ray. As a result, the estimated kernel has difficulty aggregating 3D information in a way that guarantees geometric and appearance consistency.

In this paper, we propose a deblurred NeRF based on two physical scene priors (hereafter, **DP-NeRF**) with a novel rigid blurring kernel (RBK) and adaptive weight proposal (AWP). The RBK consists of rigid ray transformation (RRT) and coarse composition weights (CCW), which utilize explicit physical scene priors derived from the blurring process to construct a consistent 3D scene representation from blurred images. In addition, the AWP proposes fine-grained color composition weights considering the relationship between depth and blur to create more realistic and clean 3D representation. Furthermore, we propose coarse-to-fine optimization for stable training and to gradually increase the effect of the AWP during training by introducing exponential weight decay between the two losses from the RBK and AWP. Figure 1 summarizes the DP-NeRF’s system using the rigid motion of the camera.

The RBK generates a 3D deformation field and coarse weights for color composition based on the view information for each scene regardless of the pixel for each ray. This architecture is inspired by the physical scene prior that the blurring process consistently occurs for all pixels for a specific view. Specifically, the deformation field is constructed as the 3D rigid motion of the camera for each view and does not depend on the 2D spatial position of each ray. In contrast to Deblur-NeRF [22], our model successfully models 3D space with consistent geometry and appearance due to the use of these conditional physical priors and not fully depending on 2D pixel-wise independent ray optimization.

Previous studies have claimed that color composition process in a blurring kernel are affected by the depth values of the pixels when compositing blurred colors from both camera motion and defocus blur [43, 44]. Hence, RBK can lose detail in regions that have a complex depth or similar textures even though it achieves remarkably realistic 3D scene. For this reason, the AWP refines the composition weights using feature modulation (FM) [59] and novel motion feature aggregation module (MAM) based on the depth features of samples for transformed rays, the viewing direction, and the view information. Following the [22], we jointly optimize the RBK, AWP, and sharp NeRF with only the reconstruction loss from the blurred input as supervision. During inference stage, we can clearly render a recon-

structed 3D scene using only the trained sharp NeRF model.

The rest of the paper is structured as follows. In Section 3, we describe the RBK and AWP in detail. In Section 4.1 and supplementary material, we provide experimental results for novel view synthesis using synthetic and real scene datasets with two types of blur that are provided from [22]. The results show that DP-NeRF achieves significant quantitative and qualitative improvement, preserving 3D consistency with a cleanly rendered novel view. In addition, we extensively analyze the effectiveness of the proposed model in Section 4.2. We also demonstrate how the RBK approximately models the blurring process in the supplementary material. To summarize, this paper offers the following major contributions.

- *Rigid blurring kernel.* We propose a novel RBK to construct a clean NeRF from blurred images utilizing physical scene priors derived from the blurring process during image acquisition.
- *Adaptive weight proposal.* We propose an AWP to refine the composition weights in the RBK considering the relationship between depth and blur to generate more realistic results.
- *Coarse-to-fine optimization.* To fully utilize proposed methods in training, we propose coarse-to-fine optimization by applying exponential weight decay between the reconstruction loss from the RBK and AWP.
- *Significant improvement in perceptual quality.* DP-NeRF produces enhanced 3D scene representation with greater perceptual quality and clean photorealistic rendered images.

2. Related work

NeRF under various conditions. NeRF has become widespread in computer vision and graphics tasks related to neural rendering, utilizing coordinate-based implicit neural representation (INR). Due to the success of the NeRF in neural rendering, several studies have applied NeRF to other areas such as dynamic scenes [17–19, 29, 30, 33, 49, 55], generative models [28, 38], relighting [3, 23, 32, 42], human avatars [31, 45, 58], and 3D reconstruction [47, 50]. However, few studies have been conducted under non-ideal conditions [1, 2, 8, 11, 22, 25]. Mip-NeRF [1] addressed the aliasing issue of ray samples by introducing 3D conical frustum ray casting with integrated positional encoding. Mip-NeRF 360 [2] then extended Mip-NeRF [1] to unbounded 360-degree scenes using shrunken space parametrization and online distillation to improve its quality and efficiency. To address the inconsistent appearance and transient objects in the uncarefully collected images, NeRF-W [23] introduced appearance and transient latent codes to the NeRF. HDR-NeRF [8] and HDR-Plenoxel [11] modeled the high dynamic range (HDR) radiance, imitating the physical process of in-camera image acquisition. [8] modeled

camera response function with the exposure value for the NeRF and [11] modeled white balance function for Plenoxels [52]. Deblur-NeRF [22] explored a new area of research constructing a clean NeRF from blurred images, which regularly occur during image acquisition in real-scenario.

Image Deblurring. Blur can be categorized into four types: camera motion, defocus, moving object and mixed blur. Image deblurring aims to recover a sharp image from images degraded by these types of blur. The recovery process can be expressed as to solve the equation: $B = I * K$, where B , I , and K denote the blurred image, sharp image, and blurring kernel, respectively. Deblurring can be divided into two categories, non-blind and blind, whose difference is whether the blurring kernel is known or not. Recent studies have focused primarily on blind deblurring because the blurring kernel is typically unknown in real-scenarios.

Several traditional image deblurring techniques [9, 10, 14, 39] have been proposed based on maximum a posterior (MAP) estimation [20, 34] based on a prior condition derived from natural images as a form of regularization. [39] uses global and local image priors as two piece-wise continuous functions and local smoothness constraints, while [9] proposes generalized transparency to efficiently estimate the blur filter by selecting useful pixels based on new transparency map. [10, 14] propose a sparse prior derived from local color statistics and a regularization function as the ratio of the l1-norm to the l2-norm for the high frequencies of an image, respectively.

Recently, deep image deblurring has been investigated following the success of deep learning networks in computer vision field. In this approach, a general blurring kernel is usually employed and latent images constructed based on blind deblurring and a data-driven prior through network training with paired datasets. Several studies have been proposed the use of convolutional neural network(CNN) [27, 46, 48, 53, 54] and generative models [15, 16]. We focus on priors from traditional methods because physical priors are helpful for constructing a blurring kernel in a NeRF system.

NeRF from Blurred Images. Deblur-NeRF [22] models the blurring kernel with the NeRF imitating the blind deblurring to produce clean and sharp NeRF. In contrast to recent deblurring methods that operate in the image space, the target blur types are camera motion and defocus blur in a static scene. Motion blur is excluded as a separate problem that needs to be overcome because temporal inconsistency is another challenge in 3D reconstruction. In [22], blurring kernel is optimized based on the kernel points on the 2D image pixels and view-embedded information. The kernel is designed around transformed rays that penetrate the kernel points on the image plane and camera origin, which are independently optimized during the training. However, the kernel relies heavily on the training of the deep neural network without cues for geometric and appearance consistency

in 3D scene representation, which leads to a lack of consistency in 3D scene. Our method focuses on this limitation and proposes a novel blurring kernel with two physical priors derived from physical process of blur acquisition and ray casting as a form of regularization for kernel estimation.

3. Deblurred Neural Radiance Field

In this section, we describe our process for constructing a clean NeRF given a set of blurred inputs. Initially, we model the RBK to use the blur consistency in an image as a physical scene priors(Section 3.2). To consider the relationship between depth and blur, we then model the AWP module(Section 3.3). Finally, we explain our loss function and coarse-to-fine optimization strategy for the training of DP-NeRF(Section 3.4). Overall process for DP-NeRF is summarized in Figure 10.

3.1. Preliminary

Neural Radiance Field (NeRF). NeRF [26] constructs a continuous, volumetric representation of a 3D scene based on INR. It uses a multi layer perceptron(MLP) to approximate the function

$$F : (\gamma_{\mathbf{x}}(\mathbf{x}), \gamma_{\mathbf{d}}(\mathbf{d})) \rightarrow (\mathbf{c}, \sigma), \quad (1)$$

which maps 3D position $\mathbf{x} = (x, y, z)$ and viewing direction $\mathbf{d} = (\phi, \theta)$ to a color $c = (r, g, b)$ and volume density σ .

Specifically, the 3D position and viewing direction are independently projected to a higher dimension by applying the sinusoidal positional encoding function $\gamma : \mathbb{R}^3 \rightarrow \mathbb{R}^{3+6m}$, which is defined as

$$\gamma(\mathbf{x}) = (\mathbf{x}, \dots, \sin(2^f \pi \mathbf{x}), \cos(2^f \pi \mathbf{x}), \dots), \quad (2)$$

where $f = \{0, \dots, m-1\}$ and m is a hyper-parameter that decides the frequency band. For clarity, we abbreviate the positional encoding and represent the NeRF as

$$F(\mathbf{x}, \mathbf{d}) = (\mathbf{c}, \sigma). \quad (3)$$

To train the NeRF with input images, the NeRF renders each color \hat{C}^p of pixel p using a rendering technique [24] that is an approximated version of classical volume rendering [12]. For given ray origin \mathbf{o}^p and viewing direction \mathbf{d}^p along a pixel p , the i_{th} sample on the ray \mathbf{r}^p is defined as $\mathbf{r}_i^p = \mathbf{o}^p + t_i \mathbf{d}^p$, where t_i is drawn from N evenly spaced bins with stratified sampling [26] in near-to-far bounded partition $[t_n, t_f]$ as shown in Eq. 4:

$$t_i \sim \mathcal{U} \left[t_n + \frac{i-1}{N} (t_f - t_n), t_n + \frac{i}{N} (t_f - t_n) \right]. \quad (4)$$

Pixel color \hat{C}^p is computed from the predicted color \mathbf{c}_i^p and density σ_i^p of each sample \mathbf{r}_i^p as shown in Eq. 5:

$$\hat{C}(\mathbf{r}) = \sum_{i=1}^N w_i \mathbf{c}_i = \sum_{i=1}^N T_i (1 - \exp(-\sigma_i \delta_i)) \mathbf{c}_i, \quad (5)$$

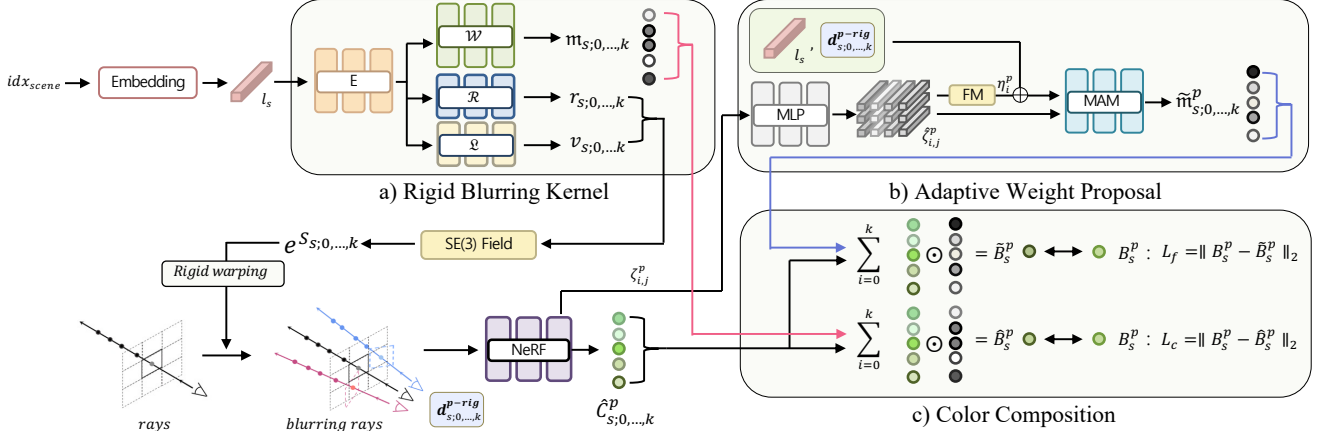


Figure 2. Overall pipeline for DP-NeRF. DP-NeRF consists of three stages. (a) The rigid blurring kernel (RBK) constructs the blurring system using the $SE(3)$ Field based on the physical priors. (b) The adaptive weight proposal (AWP) refines the composition weights using the depth feature ($\zeta_{i,j}^p$) of the samples on the ray of the target pixel (p), the scene (s) information, and the rigidly transformed ray directions ($\mathbf{r}_{s;0,\dots,k}^p$). (c) Finally the coarse and fine blurred colors, \hat{B}^p and \tilde{B}^p , are composited using the weighted sum of the ray transformed colors. \mathcal{L}_c and \mathcal{L}_f denote the coarse and fine RGB reconstruction loss, respectively.

where $T_i = \exp(-\sum_{j=1}^{i-1} \sigma_j \delta_j)$ is the transmittance and $\delta_i = t_{i+1} - t_i$ is the distance between adjacent samples. Note that, we abbreviate the notation for pixel p for clarity.

Blind Deblurring in the NeRF. Our goal is to solve the blind deblurring process with respect to sharp pixel color \hat{C}^p and blurring kernel h^p in a similar manner to [22] as

$$\hat{B}^p = \hat{C}^p * h^p, \quad (6)$$

where \hat{C}^p is computed from sample color \mathbf{c}_i^p and density σ_i^p , which are predicted by the NeRF. [22] models kernel h^p by introducing approximated n sparse kernel points in $K \times K$ sized window $\mathcal{N}(p)$ at the 2D pixel location, which are optimized by the MLP. The rendered pixel colors from the kernel points are then composited by the corresponding weights w_q^p , which are also predicted by the MLP, as Eq. 7:

$$\hat{B}^p = \sum_{q \in \mathcal{N}(p)} w_q^p \hat{C}_q^p \quad (7)$$

The kernel points and weights for each pixel ray are optimized independently depending on the 2D spatial pixel coordinates and view-information. Thus, the blurring kernel is dynamic, but they overlook the importance of geometric and appearance consistency in overall 3D space.

3.2. Rigid Blurring Kernel (RBK)

Physical Scene Priors. As we mentioned in Section 3.1, deblurring in the NeRF should consider 3D consistency. To address this, we impose two priors as constraints inspired by the physical process of image blurring.

Prior 1: A blurred image is generated during in-camera image acquisition. The first prior shares ray rigid transformation (RRT) from camera motion through all of the pixels of a blurred image because same camera is used.

Prior 2: The blurring process for all of the pixels in a blurred image occurs simultaneously. The second prior

shares the coarse composition weights (CCW) across all of the pixels of an image because the color composition of all of the pixels in a blurred image is affected simultaneously.

Ray Rigid Transformation. From the first prior, we mimic the blurring process of an image using RRT based on each image’s view information. RRT is formulated as ray transformation derived from the deformation of rigid camera motion, defined as the dense $SE(3)$ field for scene s , approximated by the MLPs, which consists of shared encoder MLP E and independent MLPs (\mathcal{R} and \mathcal{L}), as shown in Eq. 8:

$$\mathcal{S}_s = (\mathcal{R}(E(l_s)); \mathcal{L}(E(l_s))), \text{ where } s \in N_{img}, \quad (8)$$

where l_s denotes the latent code for each scene through the embedding layer [4], and N_{img} denotes a set of image indices. The scene-wise $SE(3)$ field can encode the rigid motion of the camera for the scene, thus consistently transforming the rays of the scene to imitate the blurring process. Inspired by Nerfies [29], rigid motion is encoded as the screw axis [21] $\mathcal{S}_s = (r_s; v_s) \in \mathbb{R}^6$, where $r_s \in \mathfrak{so}(3)$ encodes rotation. $\hat{r}_s = r_s / \|r_s\|$ is the axis of rotation and $\theta = \|r_s\|$ is the angle of rotation. Rotation matrix $e^{r_s} \in SO(3)$ is taken from Rodrigues’ formula [35]:

$$e^{r_s} \equiv e^{[r_s]} = \mathbf{I} + \frac{\sin \theta}{\theta} [r_s]_{\times} + \frac{1 - \cos \theta}{\theta^2} [r_s]_{\times}^2, \quad (9)$$

where $[x]_{\times}$ denotes the cross-product matrix of vector x . The translation matrix, which is encoded by screw motion \mathcal{S}_s , is taken as $\mathbf{p}_s = \mathbf{G}_s v_s$, where

$$\mathbf{G}_s = \mathbf{I} + \frac{1 - \cos \theta}{\theta^2} [r_s]_{\times} + \frac{\theta - \sin \theta}{\theta^3} [r_s]_{\times}^2. \quad (10)$$

For given ray \mathbf{r}_s^p on arbitrary pixel p in scene s , we can define the RRT as

$$\mathbf{r}_{s;q}^{p-rig} = e^{\mathcal{S}_{s;q}} \mathbf{r}_s^p = e^{\mathcal{S}_{s;q}} \mathbf{r}_s^p = e^{r_{s;q}} \mathbf{r}_s^p + \mathbf{p}_{s;q}, \quad (11)$$

where $q \in \{1, \dots, k\}$, k is a hyper-parameter that controls the number of camera motions contributing to the blur in

scene s , and $\mathbf{r}_{s;q}^{p-riq}$ denotes the rigidly transformed (RT) ray from \mathbf{r}_s^p . Note that, $\mathcal{S}_{s;q}^p = \mathcal{S}_{s;q}$ due to our first prior. To ensure that, for $\mathfrak{se}(3)$, $e^{\mathcal{S}_{s;q}}$ is the identity when $\mathcal{S}_{s;q} = 0$, we initialize the weights of the last layer of MLP \mathcal{R} from $\mathcal{U}(-10^{-5}, 10^{-5})$ following [29]. The transformed sharp colors $\hat{C}_{s;q}^{p-riq}$ are then rendered from $\mathbf{r}_{s;q}^{p-riq}$ using a volume-rendering technique to composite the blurry color \hat{B}_s^p based on the CCW described in the following section.

Coarse Composition Weights. From the second prior, we model the CCW field for scene s from the MLP \mathcal{W} , which shares the encoding MLP E with other MLPs (\mathcal{R} and \mathcal{L}).

$$\mathbf{m}_{s;0,\dots,k} = \sigma(\mathcal{W}(E(l_s))), \text{ where } \sum_{i=0}^k \mathbf{m}_{s;i} = 1, \quad (12)$$

where k denotes the number of camera motions shared with the RRT. \mathbf{m}_s is the CCW for scene s . σ represents the sigmoid function. Note that, the number of \mathbf{m}_s is $k + 1$, where $\mathbf{m}_{s;0}$ is the weight for original ray \mathbf{r}_s^p . Finally, blurry color \hat{B}_s^p for pixel p in scene s , is composited by the weighted sum of the rendered colors of original ray $\hat{C}_{s;0}^p$ and RT rays $\hat{C}_{s;1,\dots,k}^{p-riq}$ using the corresponding per-scene CCW $\mathbf{m}_{s;0,\dots,k}$ as shown in Eq. 13:

$$\hat{B}_s^p = \mathbf{m}_{s;0} \hat{C}_{s;0}^p + \sum_{i=1}^k \mathbf{m}_{s;i} \hat{C}_{s;i}^{p-riq} \quad (13)$$

The RBK pipeline is summarized in Figure 10 (a) and (c).

3.3. Adaptive Weight Proposal (AWP)

Relationship between Depth and Blur. Though the proposed RBK models the blurring kernel successfully with realistic rendering results (Figure 4), there is still room for improvement in the relationship between depth and blur. Several past studies have described the relationship between depth and each type of blur [43, 44]. Specifically, camera motion blur is affected by depth when the camera motion is out-of-plane [44], while defocus blur is usually affected by depth [43]. Therefore, we employ the AWP module to alleviate the color composition errors by flexibly refining the CCW $\mathbf{m}_{s;0,\dots,k}$ along the depth features of the samples on the original and RT rays for pixel p . Further description for motivation of AWP is attached in supplementary material.

AWP Network. We define the AWP as a function that infers the per-pixel adaptive composition weights $\tilde{\mathbf{m}}_{s;0,\dots,k}^p$ utilizing the depth features of each sample on the rays, corresponding to the latent code of each scene, and the direction of each ray. The function \mathcal{AWP} is defined as Eq. 14:

$$\tilde{\mathbf{m}}_{s;0,\dots,k}^p = \mathcal{AWP}(\zeta_{s;0,\dots,k}^p; j=1,\dots,N, \mathbf{d}_{i=0,\dots,k}^{p-riq}, l_s), \quad (14)$$

where i denotes the original and RT rays, and j denotes the sample on each ray. In addition, ζ denotes the corresponding depth feature and $\mathbf{d}_{0,\dots,k}^{p-riq}$ denotes the directions of original and RT rays. We then composite the adaptive blurred color \hat{B}_s^p through $\tilde{\mathbf{m}}_{s;0,\dots,k}^p$ as shown in Eq. 15:

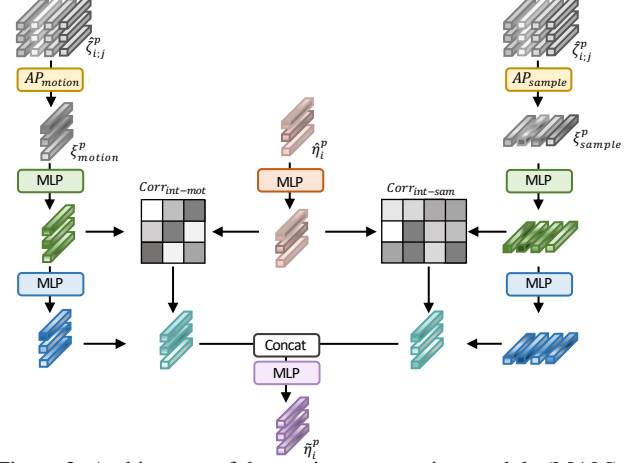


Figure 3. Architecture of the motion aggregation module (MAM).

$$\tilde{B}_s^p = \tilde{\mathbf{m}}_{s;0}^p \hat{C}_{s;0}^p + \sum_{i=1}^k \tilde{\mathbf{m}}_{s;i}^p \hat{C}_{s;i}^{p-riq} \quad (15)$$

We design \mathcal{AWP} to be an approximation using a deep learning network (Figure 10 (b) and (c)).

Network Architecture. Inspired by CurveNet [51], the AWP generates the fine weights $\tilde{\mathbf{m}}_{s;i}^p$ utilizing the inter-sample and inter-motion correlation of the rays transformed by the RBK, which are denoted as $Corr_{int-sam}$ and $Corr_{int-mot}$ in Figure 11, respectively. The depth features for each sample on the rays ($\zeta_{i;j}^p$) are extracted from second-to-last layer of the NeRF, which contains implicit occupancy information. First, we construct motion-wise modulated features, $\eta_{i=0,\dots,k}^p$, through feature modulation (FM) [59] from N samples on each ray as shown in Figure 10 (b) and Eq. 16:

$$\eta_i^p = \sum_{l=1}^N \left(\exp\left(-\sum_{m=1}^{l-1} \delta_m \hat{\zeta}_{i;m}^p \circ (1 - \exp(-\delta_l \hat{\zeta}_{i;l}^p)) \circ \hat{\zeta}_i^p\right) \right), \quad (16)$$

where $\hat{\zeta}_{i;j}^p$ denotes the embedded features of $\zeta_{i;j}^p$ from the simple MLP and δ is the same as in Eq. 5. Second, we add the viewing direction and scene-information by using a simple MLP with η_i^p , $\mathbf{d}_{i=0,\dots,k}^{p-riq}$, and l_s , as shown in Eq. 17:

$$\hat{\eta}_i^p = MLP\left(\eta_i^p, \gamma_{\mathbf{a}}(\mathbf{d}_i^{p-riq}), l_s\right), \text{ where } i \in \{0, \dots, k\}, \quad (17)$$

where $\hat{\eta}_i^p$ denotes the modulated features with the viewing information. We then forward ($\zeta_{i;j}^p$ and $\hat{\eta}_i^p$) to the MAM to aggregate the implicit depth-derived information based on attentive feature extraction as in Eq. 18:

$$\tilde{\eta}_i^p = MAM(\zeta_{i;j}^p, \hat{\eta}_i^p), \quad (18)$$

where $\tilde{\eta}_i^p$ denotes the aggregated features.

For the MAM, we first generate motion-wise and sample-wise representative features, $\xi_{s;motion}^p$ and $\xi_{s;sample}^p$, by forwarding the embedding MLP and employing attentive pooling [7] along each axis from the embedded features $\zeta_{i;j}^p$. Note that, we omit the embedding MLP in Figure 11 for clarity. Second, we compute the inter-motion

and inter-sample correlation using CurveNet-like architecture via matrix multiplication. Third, the correlated features update each embedded features using matrix multiplication. Finally, aggregated features $\hat{\eta}_i^p$ are extracted by concatenating the correlated embedded features and forwarding the simple MLP. The overall process for the MAM is described as Figure 11 and Eq. 24:

$$MAM(\hat{\xi}_{i;j}^p, \hat{\eta}_i^p) = MLP(cat(\mathbf{corr}(\hat{\eta}_i^p, \xi_{motion}^p, \xi_{sample}^p))), \quad (19)$$

where cat denotes the concatenating operation and \mathbf{corr} represents computing operations of inter-motion and inter-sample correlation. To this end, the adaptive composition weights $\tilde{m}_{s;0,\dots,k}^p$ are predicted using global average pooling (GAP) along the motion axis and the linear layer as shown in Eq. 20. We omit the GAP and the final Linear layer for clarity in Figure 10 (b).

$$\tilde{m}_{s;i}^p = \sigma(Linear(GAP(\tilde{\eta}_{i=0,\dots,k}^p))), \text{ where } \sum_{i=0}^k \tilde{m}_{s;i}^p = 1 \quad (20)$$

Details of the operation and notations for the feature dimensions are presented in the supplementary material.

3.4. Training & Optimization

Training Loss. DP-NeRF takes only the RGB reconstruction loss for the blurred color of a pixel with a corresponding ray because our goal is to approximate the blurred color of the pixel using the RBK and AWP. In contrast to Deblur-NeRF [22], we employ two blurred colors \hat{B}_s^p and \tilde{B}_s^p to optimize the DP-NeRF. Our RGB reconstruction loss \mathcal{L}_{recon} consists of two reconstruction losses from these predicted colors and the ground truth color as shown in Eq. 21:

$$\mathcal{L}_{recon} = \|B_s^p - \hat{B}_s^p\| + \|B_s^p - \tilde{B}_s^p\|, \quad (21)$$

where B_s^p and \mathcal{L} denote the ground truth blurred RGB for pixel p and the loss function, respectively.

Coarse-to-Fine Optimization. However, it is difficult to simultaneously optimize the loss function from scratch due to the complex geometry and texture of 3D scenes. Hence, we propose a coarse-to-fine optimization strategy for the two losses by introducing coarse-to-fine weight λ , which exponentially decays from λ_s to λ_e during training as shown in Eq. 22:

$$\begin{aligned} \alpha &= -\log(\lambda_s/\lambda_e)/(e_f - e_c), \\ \lambda &= \lambda_s(\exp(\alpha(e_c - e_i))), \end{aligned} \quad (22)$$

where e_c , e_i , and e_f denote the current, initial, and final iteration of the training process, respectively. Therefore, our final loss function \mathcal{L}_{final} is defined as shown in Eq. 23:

$$\mathcal{L}_{final} = \lambda\|B_s^p - \hat{B}_s^p\| + (1 - \lambda)\|B_s^p - \tilde{B}_s^p\|, \quad (23)$$

where the first and second terms without λ and $(1 - \lambda)$ are denoted as \mathcal{L}_c and \mathcal{L}_f in the caption of Figure 10, referring to coarse and fine RGB reconstruction loss, respectively.

4. Experiment

Implementation Details. DP-NeRF is implemented using official code published for a previous work [22]. Note that, our blur operation should be applied to scene irradiance instead of image intensity, as pointed out by [5], following [22]. Hence, a tone mapping function is applied to the predicted radiance color from the NeRF in the same manner as the gamma function in [22]. For fair comparison with [22], we set the default configuration to be same as in that study. The number of camera motions k is set to 4 as the default because the number of kernel points in [22] is set to 5. We use a batch size of 1024 rays, with 64 coarse samples, and 64 fine samples on the rays. We use the Adam [13] optimizer with default parameters. For the scheduling learning rate, we exponentially weight decay from 5×10^{-4} to 8×10^{-5} . In addition, we set λ_s and λ_e at 0.9 and 0.1 for the coarse-to-fine optimization, respectively. We also use $200k$ iterations to train each scene. Further details are provided in the supplementary material.

Datasets. We train DP-NeRF using the synthetic and real scene datasets provided by [22]. Both dataset consist of two blur types: camera motion and defocus blur. There are five scenes in the synthetic dataset and ten in the real dataset for each blur type. The camera poses for all of the images are calibrated using COLMAP [36, 37]. As mentioned in [22], the real scenes were manually captured with a Canon EOS RP under manual exposure mode.

4.1. Novel View Synthesis

Evaluations. In this section, we summarize the results of our model for the synthetic and real scenes. The quantitative quantitative and qualitative results for the synthetic dataset are presented in Table 1 and Figure 4. Three commonly used evaluation metrics are adopted in the present study to compare the synthesized and ground truth images: the peak signal-to-noise ratio (PSNR), the structural similarity index measure (SSIM), and learned perceptual image patch similarity (LPIPS) [56], which assess relative sharpness, structural similarity, and perceptual quality, respectively. Due to the length, we only present the average results here for the real scene dataset. A more version of the experimental results is available in the supplementary material.

Comparisons. Tables 1 and 2 show that our model produces excellent results for all metrics compared to the other models, including [22]. In particular, LPIPS is significantly improved by DP-NeRF, indicating a 3D scene with a higher rendered image quality in terms of perceptual quality. Note that, the results for single image deblurring methods, MPR+NeRF, PVD+NeRF, and KPAC+NeRF, in Tables 1 and 2 are taken from [22]. They are trained with a Naive NeRF using images deblurred using MPR [53], PVD [41], and KPAC [40] methods, respectively.

Camera Motion	Factory			Cozyroom			Pool			Tanabata			Trolley			Average		
	PSNR(\uparrow)	SSIM(\uparrow)	LPIPS(\downarrow)	PSNR(\uparrow)	SSIM(\uparrow)	LPIPS(\downarrow)	PSNR(\uparrow)	SSIM(\uparrow)	LPIPS(\downarrow)	PSNR(\uparrow)	SSIM(\uparrow)	LPIPS(\downarrow)	PSNR(\uparrow)	SSIM(\uparrow)	LPIPS(\downarrow)	PSNR(\uparrow)	SSIM(\uparrow)	LPIPS(\downarrow)
Naive NeRF [26]	19.32	.4563	.5304	25.66	.7941	.2288	30.45	.8354	.1932	22.22	.6807	.3653	21.25	.6370	.3633	23.78	.6807	.3362
MPR [53] + NeRF	21.70	.6153	.3094	27.88	.8502	.1153	30.64	.8385	.1641	22.71	.7199	.2509	22.64	.7141	.2344	25.11	.7476	.2148
PVD [41] + NeRF	20.33	.5386	.3667	27.74	.8296	.1451	27.56	.7626	.2148	23.44	.7293	.2542	23.81	.7351	.2567	24.58	.7190	.2475
Deblur-NeRF [22]	25.60	.7750	.2687	32.08	.9261	.0477	31.61	.8682	.1246	27.11	.8640	.1228	27.45	.8632	.1363	28.77	.8593	.1400
DP-NeRF	25.91	.7787	.2494	32.65	.9317	.0355	31.96	.8768	.0908	27.61	.8748	.1033	28.03	.8752	.1129	29.23	.8674	.1184

Defocus	Factory			Cozyroom			Pool			Tanabata			Trolley			Average		
	PSNR(\uparrow)	SSIM(\uparrow)	LPIPS(\downarrow)	PSNR(\uparrow)	SSIM(\uparrow)	LPIPS(\downarrow)	PSNR(\uparrow)	SSIM(\uparrow)	LPIPS(\downarrow)	PSNR(\uparrow)	SSIM(\uparrow)	LPIPS(\downarrow)	PSNR(\uparrow)	SSIM(\uparrow)	LPIPS(\downarrow)	PSNR(\uparrow)	SSIM(\uparrow)	LPIPS(\downarrow)
Naive NeRF [26]	25.36	.7847	.2351	30.03	.8926	.0885	27.77	.7266	.3340	23.80	.7811	.2142	22.67	.7103	.2799	25.93	.7791	.2303
KPAC [40] + NeRF	26.40	.8194	.1624	28.15	.8592	.0815	26.69	.6589	.2631	24.81	.8147	.1639	23.42	.7495	.2155	25.89	.7803	.1773
Deblur-NeRF [22]	28.03	.8628	.1127	31.85	.9175	.0481	30.52	.8246	.1901	26.26	.8517	.0995	25.18	.8067	.1436	28.37	.8527	.1188
DP-NeRF	29.26	.8793	.1035	32.11	.9215	.0386	31.44	.8529	.1563	27.05	.8635	.0779	26.79	.8395	.1170	29.33	.8713	.0987

Table 1. Quantitative results for the synthetic scene. Each color shading indicates the **best** and **second-best** result, respectively.

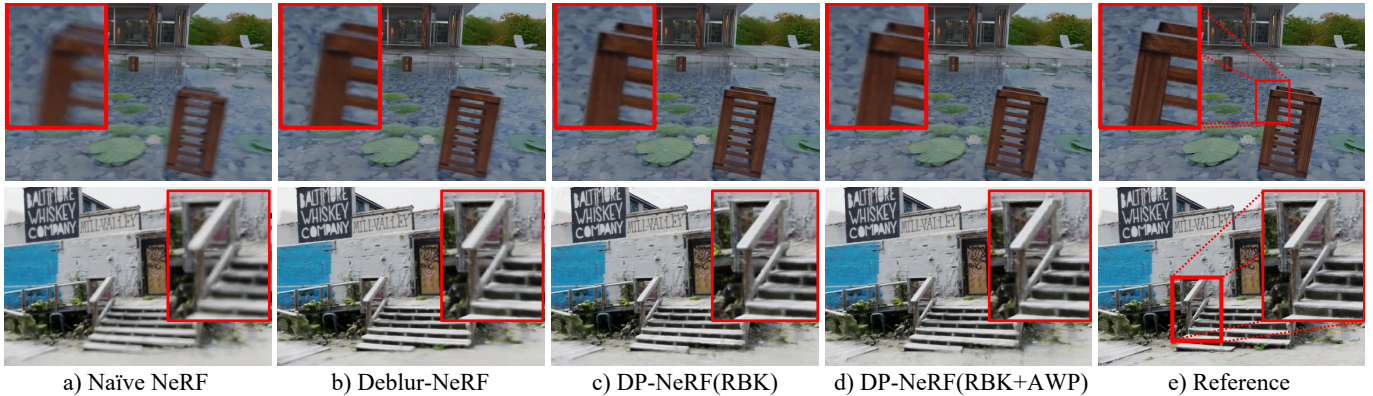


Figure 4. Rendered novel view synthesis results of DP-NeRF for synthetic scenes. Top and bottom row denote results of camera motion and defocus blur scene, respectively. Figure (a)-(e) denote Naive NeRF, Deblur-NeRF, DP-NeRF (RBK), DP-NeRF (RBK+AWP), and ground truth images, respectively. Each colored box in corner of images are enlarged parts of the colored box region in reference images.

Camera Motion	Defocus		
	PSNR(\uparrow)	SSIM(\uparrow)	LPIPS(\downarrow)
Naive NeRF [26]	22.69	.6347	.3687
MPR [53] + NeRF	23.38	.6655	.3140
PVD [41] + NeRF	23.10	.6389	.3425
Deblur-NeRF [22]	25.63	.7675	.1820
DP-NeRF	25.91	.7751	.1602

Defocus	Camera Motion		
	PSNR(\uparrow)	SSIM(\uparrow)	LPIPS(\downarrow)
Naive NeRF [26]	22.40	.6661	.2310
KPAC [40] + NeRF	23.04	.6917	.1847
Deblur-NeRF [22]	23.46	.7199	.1207
DP-NeRF	23.67	.7299	.1082

Table 2. Average results for the real scene dataset. Each color shading indicates the **best** and **second-best** result, respectively.

The qualitative results presented in Figure 4 demonstrate the effectiveness of DP-NeRF. The RBK more successfully models a clean 3D scene representation with geometric and appearance consistency compared to previous approaches. It more cleanly reproduces the structure of the object in the scene compared to Naive NeRF and Deblur-NeRF.

4.2. Ablation Study

Effectiveness of the RBK and AWP. The DP-NeRF successfully constructs clean NeRF with geometric and appearance consistency using RBK and AWP as shown in Figure 4. The RBK by itself still has difficulty in inferring the correct texture and geometry in some regions in which the texture is confused with the background, the structure is thin, or the depth is complex, as indicated by the red box in Figure 4 (c). However, the rendered results in Figure 4 (d) demonstrate that the AWP effectively refines the geometric

and appearance consistency in this region. In particular, the upper and lower rows exhibit detailed enhancement of the geometric structure and texture of the edge of the box and stairs, respectively.

To understand the effectiveness of DP-NeRF more clearly, Figure 5 present an error map visualization of the stairs scene, with the brighter colors indicating greater error. DP-NeRF produces a lower error than the baselines, reconstructing the fine details of the objects in the scene. We also provide additional error map images without the red boxes in the supplementary material, including those for another type of blur in synthetic scenes.

The Number of Rigid Motions. Figure 6 presents ablation analysis for the number of rigid motions, which defines the number of transformed rays, for the two types of the blur. We use LPIPS as the evaluation metric because it represents perceptual quality well, as demonstrate in Nerfies [29]. The results show that the performance of the RBK and RBK+AWP improves as the number of rigid motions increases, while the LPIPS for RBK+AWP is better than that for the RBK alone in all experiments. Full quantitative PSNR, SSIM, and LPIPS results and qualitative results for the RBK and RBK+AWP are additionally presented in the supplementary material.

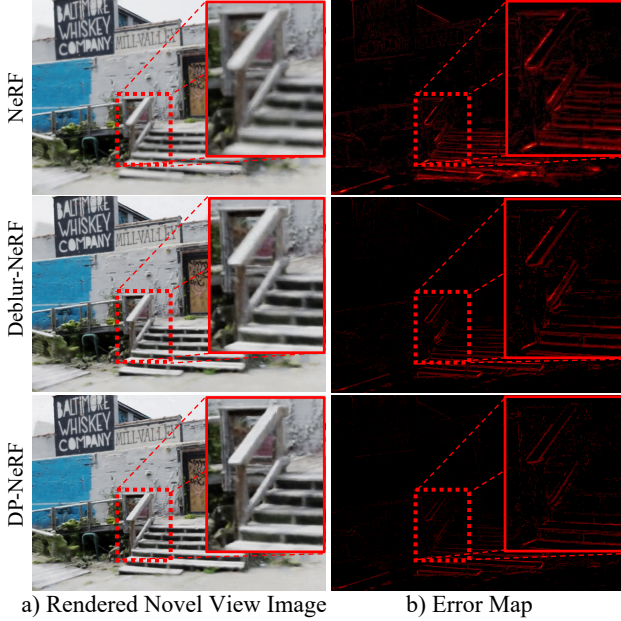


Figure 5. Visual comparison with error maps of NeRF, Deblur-NeRF, and DP-NeRF (ours) in defocus **Factory** scene. Regions with red box indicate emphasized regions of error map.

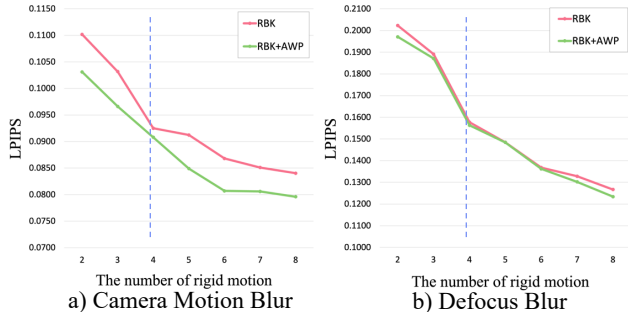


Figure 6. Ablation analysis on the number of rigid camera motions for the two types of blur for synthetic **Pool** scene. (a) and (b) show the results on camera motion and defocus blur, respectively. magenta and yellowgreen colors indicate results of RBK and RBK+AWP, respectively. blue color line indicates the results when the number of rigid motions is 4, which is same as of the kernel points 5 in Deblur-NeRF [22] for fair comparison in Table 1.

RBK Analysis. The RBK is shown to successfully model the blur derived from both camera movement and a change in the focus plane as the rigid motion of the camera. We demonstrate the validity of the RBK design by presenting additional kernel analysis in the supplementary material.

5. Limitation & Future Work

Temporal Motion Blur. Our model fails when object motion blur is present in a scene (Figure 7). Though DP-NeRF produces images of higher quality than does a standard NeRF, motion blur still occurs in reconstructed scenes because we impose the physical priors based on the assumption of a static scene. Object motion blur is an issue associated with temporal information and there is no multi-view data for a specific time in the given dataset. This dataset

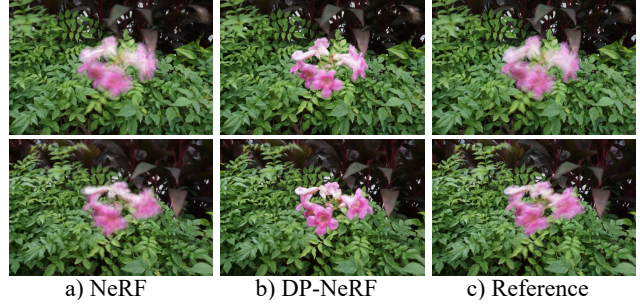


Figure 7. Visual comparison for the NeRF, the DP-NeRF, and the reference image at specific time on object motion blur. There are still artifacts in region where motion blur occurred.

structure leads to inherent geometric and appearance inconsistency in the 3D scene if we construct the NeRF without temporal modeling. Therefore, we are confident that this limitation can be addressed with an additional temporal component in DP-NeRF in the future, such as bending the rays with $SE(3)$ field warping [29], scene flow [18], or 3D displacement [33] on ray samples. Actually, although Figure 7 (b) seems to be quite clean, the results show the explicit inconsistency when we render the spiral video to assess the 3D consistency. Please refer the rendered videos in our project page to check the temporal inconsistency.

Various Types of Image Noise. As mentioned in Section 2, several previous studies have addressed other types of image noise for NeRF, such as temporal and exposure variation. The modeling for these noise could be integrated with the DP-NeRF system because they are independent of each other, including our target noise. This can be addressed in the future research if an appropriate dataset is constructed.

6. Conclusion

This paper proposes DP-NeRF, a novel NeRF framework from blurry inputs, that imposes the two physical priors to effectively construct a clean NeRF. We propose the RBK to maintain geometric and appearance consistency in continuous 3D space. In addition, We employ the AWP module to alleviate the color composition errors by considering the relationship between depth and blur. We also introduce coarse-to-fine optimization of the two losses from the proposed modules to effectively utilize both during the training process. Extensive experiments using synthetic and real scene datasets verified that DP-NeRF produces an improved, clean NeRF with high perceptual quality and 3D consistency in terms of geometry and appearance. We believe that DP-NeRF represents an advance in NeRF and can be used in conjunction with other methods to construct clean NeRF, covering the images with other types of noise.

Acknowledgements. This work was supported by Institute of Information & communications Technology Planning & Evaluation (IITP) grant funded by the Korea government(MSIT) (No.2021-0-02068, Artificial Intelligence Innovation Hub) and the Yonsei University Research Fund of 2021 (2021-22-0001).

Appendix

A. Additional Implementation Details

A.1. Training

DP-NeRF is implemented on two Nvidia RTX 3090 GPUs based on the published code and dataset for Deblur-NeRF [22] using PyTorch [?]. Training images are resized to 600×400 across the entire dataset to train the DP-NeRF. In addition, we start to optimize proposed components, rigid blurring kernel (RBK), adaptive weight proposal (AWP), and color composition (CC), after 1200 training iterations with a pure NeRF [26] to obtain coarse scene representation.

A.2. Architectural Detail

Figures 8, 9, 10, and 11 describe the DP-NeRF architecture to describe in detail. View information l_s for each image is embedded with 64 channels in a simple embedding layer.

Rigid Blurring Kernel (RBK). As shown in Figure 8, RBK consists of one shared encoding branch E and three decoding branches with simple MLPs (\mathcal{W} , \mathcal{R} , and \mathcal{L}). Encoding branch E consists of an MLP with four fully-connected linear layers, with each layer having 64 dimensions and ReLU activation function. Decoding branches for $m_{s;0,\dots,k}$, r_s , and v_s also consist of an MLP with one linear layer with 32 dimensions and an output linear layer. The output channel dimensions for $m_{s;0,\dots,k}$, r_s , and v_s is k , $3k$, and $3k$, respectively, where k is a hyper-parameter that controls the number of rigid camera motions. Note that, $m_{s;0,\dots,k}$ is normalized along the motion axis k to ensure $\sum_{i=0}^k m_{s;i} = 1$.

Adaptive Weight Proposal (AWP). First of all, we additionally describe a motivation of the complex architecture design of AWP. Intuition of AWP architecture is to fully use the spatial occupancy information of samples on the rays. When we use the similar module based on inter-motion correlation with rendered depth values on each rays, we could not get the improved results. The reason was supposed to be insufficient occupancy information of one scalar rendered depth value per ray. Hence, we design AWP to fully reflect the information to use rich correlation between the rays. Here are description of AWP architecture with detailed notations. Please refer to Figure 9, Figure 11, and Table 3 for architecture design and corresponding notations. Note that, we omit the notation for the batch dimension for clarity. Before forwarding to motion aggregation module (MAM), extracted depth feature $\zeta_{i,j}^p \in \mathbb{R}^{N_m \times N_s \times C_{d1}}$ from the second-to-last layer of the NeRF is embedded in $\hat{\zeta}_{i,j}^p \in \mathbb{R}^{N_m \times N_s \times C_{d2}}$ via the simple four-layered MLP with ReLU activation, where N_m and N_s denote the dimensions of the motion axis and sample axis, respectively. N_m is

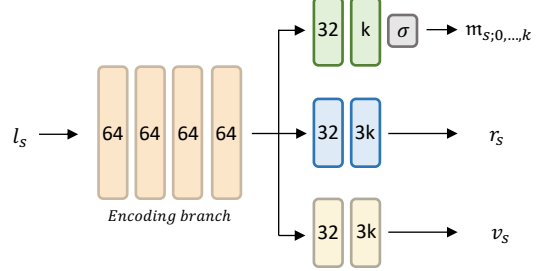


Figure 8. A detailed architecture of rigid blurring kernel (RBK).

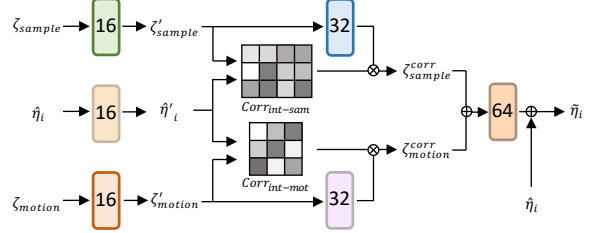


Figure 9. Detailed description about a correlation part of motion aggregation module (MAM). This picture includes process for computing correlation between ζ_{motion}^p , ζ_{sample}^p , and $\hat{\eta}_i^p$.

Notation	l_s	C_{d1}	C_{d2}	C_{d3}	C_{d4}	N_m	N_s	N_c	N_f
Value	64	128	64	32	16	$(1+k)(N_c + N_f)$	64	64	

Table 3. Notations for adaptive weight proposal (AWP) and corresponding values used in our experiment as default.

the number of blurring rays, which is a summation of the number of motion (k) and original ray (1). N_s is the total number of samples, which is a summation of the number of coarse samples (N_c) and fine samples (N_f). We then, apply feature modulation (FM) [59] to generate ray-wise representative features, $\eta_i^p \in \mathbb{R}^{N_m \times C_{d2}}$. To impose the view- and direction-information for the rays, l_s and positional embedded $\mathbf{d}_{s;0,\dots,k}^{p-rig}$ are concatenated and forwarded to the simple MLP to extract $\hat{\eta}_i^p \in \mathbb{R}^{N_m \times C_{d3}}$. To aggregate the implicit information between the modeled blurring rays, we forward $\hat{\zeta}_{i,j}^p$ and $\hat{\eta}_i^p$ to the MAM. The MAM then aggregates the extracted features from $\hat{\zeta}_{i,j}^p$ and $\hat{\eta}_i^p$ based on the computed correlation between the decomposed information along each motion and sample axis.

The MAM is formulated in the main paper as follows:

$$MAM(\hat{\zeta}_{i,j}^p, \hat{\eta}_i^p) = MLP(\text{cat}(\mathbf{corr}(\hat{\eta}_i^p, \xi_{motion}^p, \xi_{sample}^p))), \quad (24)$$

where $\zeta_{motion}^p \in \mathbb{R}^{N_s \times C_{d3}}$ and $\zeta_{sample}^p \in \mathbb{R}^{N_m \times C_{d3}}$ are embedded via a one-layer MLP and attentive pooling [7] along the motion and sample axis. Modulated feature η_i^p and attentive pooled features ζ_{motion}^p and ζ_{sample}^p are embedded again in $\hat{\eta}_i^p$, ζ_{sample}^p and ζ_{motion}^p as the same channel dimension C_{d4} before computing the correlation maps. We then compute two correlations, $Corr_{int-mot}$ and

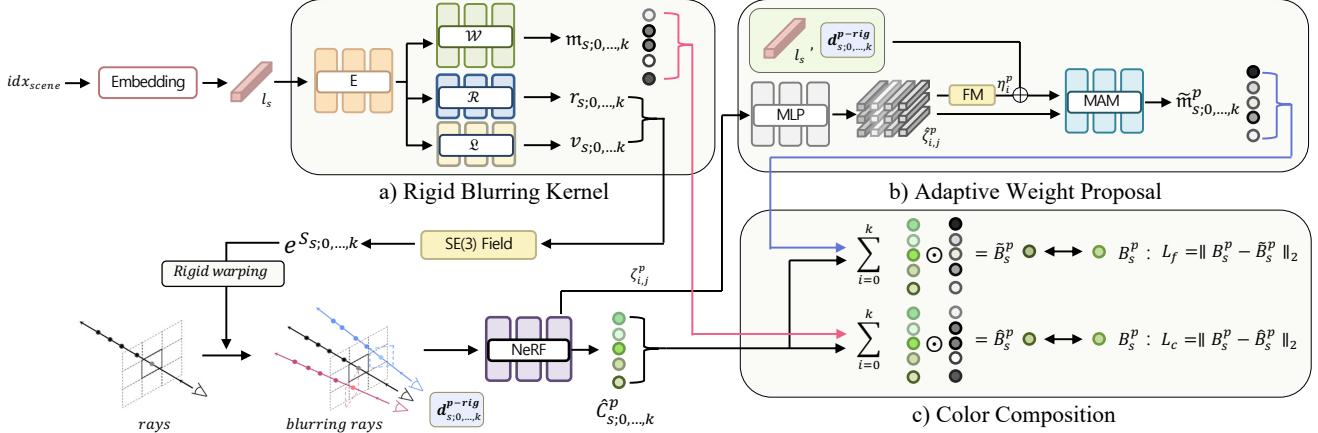


Figure 10. Overall pipeline of DP-NeRF, which is same as figure in the main paper.

$Corr_{int-sam}$, which represent the inter-motion and inter-sample correlations, respectively (Figure 9). Because $\zeta_{i,j}^p$ consists of a sample dimension and a motion dimension, we apply inter-sample and inter-motion design to investigate the inter-sample and inter-motion correlations. The each type of correlation score maps enhances the correlation of each dimension and aggregate them with modulated features via matrix multiplication. The enhanced features, ζ_{sample}^{corr} and ζ_{motion}^{corr} , are then concatenated and forwarded to the 64-channel MLP, followed by the residual connection of $\hat{\eta}_i$ to generate our final motion-aggregated feature $\tilde{\eta}_i$. Note that, the dimensions of $\hat{\eta}_i$ and $\tilde{\eta}_i$ are the same.

Tone Mapping. Before color composition for each color from the blurring rays and the composition weights $m_{s;0,\dots,k}$ or $\tilde{m}_{s;0,\dots,k}^p$, we should note that each color $\hat{C}_{s;0,\dots,k}^p$ is tone-mapped from the predicted scene irradiance from a NeRF similar to [22]. Gamma function g for the tone mapping function is simply set as shown in Eq. 25 in a similar manner to [22] because there is no significant difference in performances when either a gamma function or learnable MLP is employed as the tone mapping function.

$$g(c') = c'^{\frac{1}{2.2}}, \quad (25)$$

where c' denotes the predicted radiance from the NeRF in DP-NeRF. The types of tone-mapping function does not significantly influence the predicted radiance due to the consistent exposure of the dataset. Hence, we can rewrite the full color composition of \hat{B}_s^p and \tilde{B}_s^p as shown in Eq. 26, with g omitted in the main paper due to page limitations.

$$\begin{aligned} \hat{B}_s^p &= m_{s;0} g(\hat{C}_{s;0}^p) + \sum_{i=1}^k m_{s;i} g(\hat{C}_{s;i}^{p-rig}) \\ \tilde{B}_s^p &= \tilde{m}_{s;0}^p g(\hat{C}_{s;0}^p) + \sum_{i=1}^k \tilde{m}_{s;i}^p g(\hat{C}_{s;i}^{p-rig}) \end{aligned} \quad (26)$$

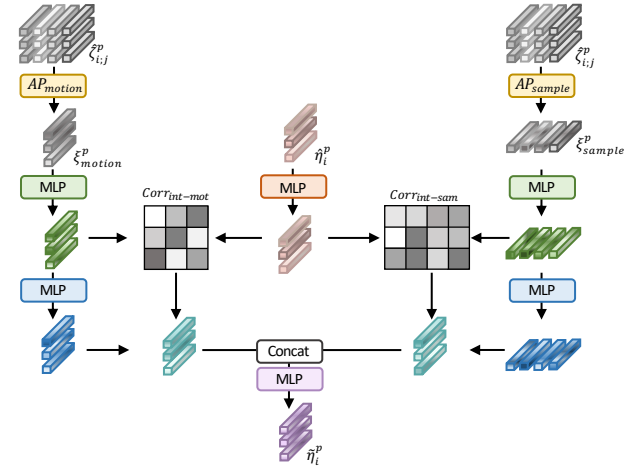


Figure 11. Architecture of motion aggregation module (MAM), which is same as figure in the main paper.

B. Evaluation Results on Real Scene

Quantitative Results. We present quantitative evaluation results for camera motion and defocus blur in the real scene dataset in Tables 4 and 5. The results show that DP-NeRF improves the quantitative performance for all of the evaluation metrics, especially on LPIPS. In addition, it is clear that PSNR and SSIM cannot fully represent the realistic perceptual quality of rendered images as argued by Nerfies [29] in their paper. Hence, the perceptual quality should be evaluated by comparing LPIPS and the rendered image quality visually.

Qualitative Results. We present the qualitative results in Figures 12 and 13. The results show that DP-NeRF(RBK) and DP-NeRF(RBK+AWP) both outperform the NeRF and baseline in terms of perceptual quality for most of the scenes. It demonstrates that our model produces more accurate 3D reconstruction quality with a realistic, clean NeRF. In addition, DP-NeRF enhances the 3D geometric and appearance consistency in several scenes. For example, due to

the complex depth and similar texture of the forest region, baselines [22, 26] have difficulty in predicting the correct geometry in the **Heron** scene (4th-row in Figure 12). However, our model predicts the region more accurately, illustrating that DP-NeRF can model complex 3D space more accurately.

C. Additional Ablation Results

C.1. RBK Analysis

Modeling Analysis. We illustrate how our RBK models camera motion and defocus blur as ray rigid transformation by presenting a visualization of the modeled kernel and rendered images from each of the transformed camera views in Figures 14 and 15. Figures 14 (a) and 15 (a) shows the transformed ray origin and direction derived from the trained DP-NeRF with paired images. Note that, each colored transformed camera origin and ray direction pairs with a rendered image with the same colored box. Each image also has the same notation as presented in the main paper ($\hat{C}_{s;0}^p$ and $\hat{C}_{s;1,\dots,k}^p$) to assist in understanding. Figures 14 (b)-(f) and 15 (b)-(f) present rendered images from the transformed cameras, which are used to composite the blurred image \tilde{B}_s^p . Figure 14 (g) and 15 (g) present the composited blurred image from images (b)-(f) with composition weights as we mentioned in the main paper. We demonstrate that the composited blurred image \tilde{B}_s^p is successfully generated, with a similar appearance to the reference image B_s^p (Figures 14 (h) and 15 (h)). Figures 14 and 15 show that DP-NeRF can model the blurred image \tilde{B}_s^p so that it is similar to reference image B_s^p for both type of the blur.

The visualizations of given ray $\mathbf{r}_s^p (= \mathbf{r}_{s;0}^p)$ and rigidly transformed (RT) rays $\mathbf{r}_{s;1,\dots,k}^{p-rig}$ in Figures 14 (a) and 15 (a) demonstrate that the camera motion and defocus blur can be successfully modeled with the RBK imitating camera movement or focus plane decision by rigidly warping the given scene camera with the $SE(3)$ field. It is obvious that camera motion blur can be successfully modeled using the RBK because it models the blurring process using rigid camera transformation. Figure 14 (a) presents the results of the camera shaking during image acquisition, which leads to camera motion blur.

Interestingly, for defocus blur, there is a plane where the RT rays intersect (Figure 15 (a)), and this is the predicted focus plane. Specifically, RBK imitates the defocus blurring by approximating the depth of field process locating the transformed rays on the virtual aperture. The predicted transforms of the rays naturally decide the focus plane as we described in Figure 15 (a). If the depth value of a given ray is not on focus plane, focus blur is naturally induced by the color composition of the given ray and the other RT rays, which penetrate the other surrounding parts of the scene.

In addition, Figures 14 (b)-(h) and 15 (b)-(h) show that

we can render images related to the construction of the blurred image for a scene. This form of image decomposition can determine how the blurred image in a scene is generated during image acquisition with respect to change in the camera settings, such as camera motion or focus plane information. Furthermore, RBK modeling guarantees the geometric and appearance consistency of each rendered image.

C.2. Effectiveness of the RBK and AWP

We present the effectiveness of the RBK and AWP with ablation analysis using the synthetic (Table 6) and real scene (Tables 7 and 8 for camera motion and defocus blur, respectively) datasets. Qualitative comparisons are also presented in Figures 12 and 13. For real scene dataset, it seems to be marginal improvement with AWP. Actually, blurring kernel is affected by the depth in case of the out-of-plane camera motion blur and general defocus blur as mentioned in [43, 44]. However, for provided camera motion blur dataset, the blur type is close to in-plane camera motion blur, which leads to the marginal improvement. In addition, shape of the blurring kernel can change depending the depth in both blur types. Instead to directly model kernel shape change, we mitigate the issue through adaptive weights between transformed rays from AWP. Our model shows the more satisfying results with geometrically clean images with RBK. In addition, we can find that our model with AWP get more detailed clean results thanks to above adaptive weights approximation.

Camera Motion	Ball			Basket			Buick			Coffee			Decoration		
	PSNR(\uparrow)	SSIM(\uparrow)	LPIPS(\downarrow)	PSNR(\uparrow)	SSIM(\uparrow)	LPIPS(\downarrow)	PSNR(\uparrow)	SSIM(\uparrow)	LPIPS(\downarrow)	PSNR(\uparrow)	SSIM(\uparrow)	LPIPS(\downarrow)	PSNR(\uparrow)	SSIM(\uparrow)	LPIPS(\downarrow)
Naive NeRF [26]	24.08	0.6237	.3992	23.72	.7086	.3223	21.59	.6325	.3502	26.48	.8064	.2896	22.39	.6609	.3633
Deblur-NeRF [22]	27.36	.7656	.2230	27.67	.8449	.1481	24.77	.7700	.1752	30.93	.8981	.1244	24.19	.7707	.1862
DP-NeRF	27.20	.7652	.2088	27.74	.8455	.1294	25.70	.7922	.1405	31.19	.9049	.1002	24.31	.7811	.1639

Camera motion	Girl			Heron			Parterre			Puppet			Stair			Average		
	PSNR(\uparrow)	SSIM(\uparrow)	LPIPS(\downarrow)	PSNR(\uparrow)	SSIM(\uparrow)	LPIPS(\downarrow)	PSNR(\uparrow)	SSIM(\uparrow)	LPIPS(\downarrow)	PSNR(\uparrow)	SSIM(\uparrow)	LPIPS(\downarrow)	PSNR(\uparrow)	SSIM(\uparrow)	LPIPS(\downarrow)	PSNR(\uparrow)	SSIM(\uparrow)	LPIPS(\downarrow)
Naive NeRF [26]	20.07	.7075	.3196	20.50	.5217	.4129	23.14	.6201	.4046	22.09	.6093	.3389	22.87	.4561	.4868	22.69	.6347	.3687
Deblur-NeRF [22]	22.27	.7976	.1687	22.63	.6874	.2099	25.82	.7597	.2161	25.24	.7510	.1577	25.39	.6296	.2102	25.63	.7675	.1820
DP-NeRF	23.33	.8139	.1498	22.88	.6930	.1914	25.86	.7665	.1900	25.25	.7536	.1505	25.59	.6349	.1772	25.91	.7751	.1602

Table 4. Quantitative results for the real scene camera motion blur. Each color shading indicates the **best** and **second-best** result, respectively.

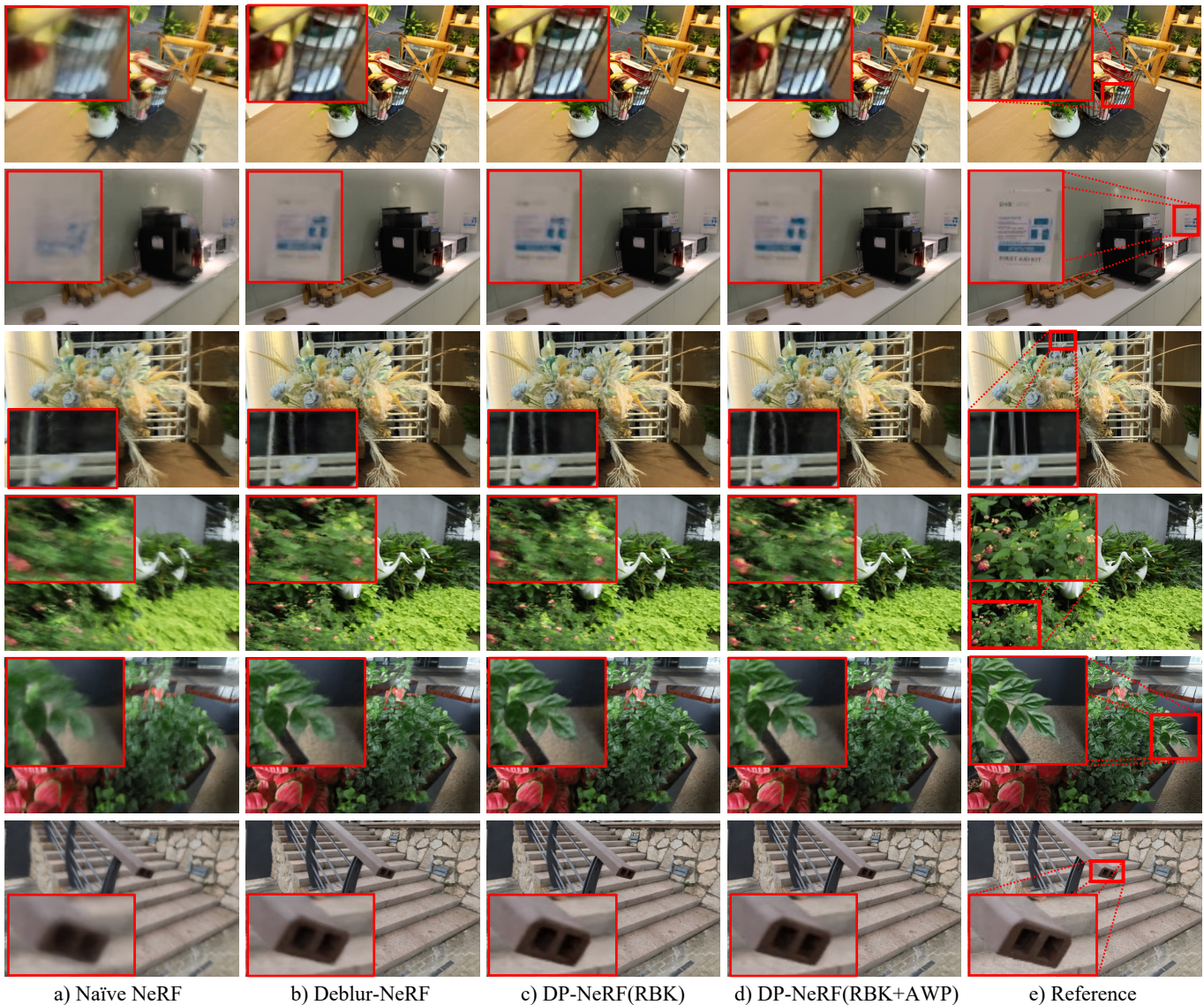


Figure 12. Rendered novel view synthesis results of DP-NeRF for real scene camera motion blur. Figures (a)-(e) denote Naive NeRF, Deblur-NeRF, ours(RBK), ours(RBK+AWP), and ground truth images, respectively. Red colored box in corner of images are enlarged part of same colored box region in reference images.

Defocus	Cake			Caps			Cisco			Cupcake			Coral		
	PSNR(↑)	SSIM(↑)	LPIPS(↓)	PSNR(↑)	SSIM(↑)	LPIPS(↓)	PSNR(↑)	SSIM(↑)	LPIPS(↓)	PSNR(↑)	SSIM(↑)	LPIPS(↓)	PSNR(↑)	SSIM(↑)	LPIPS(↓)
Naive NeRF	24.42	.7210	.2250	22.73	.6312	.2801	20.72	.7217	.1256	21.88	.6809	.2155	19.81	.5658	.2689
Deblur-NeRF [22]	26.27	.7800	.1282	23.87	.7128	.1612	20.83	.7270	.0868	22.26	.7219	.1160	19.85	.5999	.1214
DP-NeRF	26.16	.7781	.1267	23.95	.7122	.1430	20.73	.7260	.0840	22.80	.7409	.0960	20.11	.6107	.1178

Defocus	Cups			Daisy			Sausage			Seal			Tools			Average		
	PSNR(↑)	SSIM(↑)	LPIPS(↓)	PSNR(↑)	SSIM(↑)	LPIPS(↓)	PSNR(↑)	SSIM(↑)	LPIPS(↓)	PSNR(↑)	SSIM(↑)	LPIPS(↓)	PSNR(↑)	SSIM(↑)	LPIPS(↓)	PSNR(↑)	SSIM(↑)	LPIPS(↓)
Naive NeRF [26]	25.02	.7581	.2315	22.74	.6203	.2621	17.79	.4830	.2789	22.79	.6267	.2680	26.08	.8523	.1547	22.40	.6661	.2310
Deblur-NeRF [22]	26.21	.7987	.1271	23.52	.6870	.1208	18.01	.4998	.1796	26.04	.7773	.1048	27.81	.8949	.0610	23.46	.7199	.1207
DP-NeRF	26.75	.8136	.1035	23.79	.6971	.1075	18.35	.5443	.1473	25.95	.7779	.1026	28.07	.8980	.0539	23.67	.7299	.1082

Table 5. Quantitative results for the real scene defocus blur. Each color shading indicates the best and second-best result, respectively.

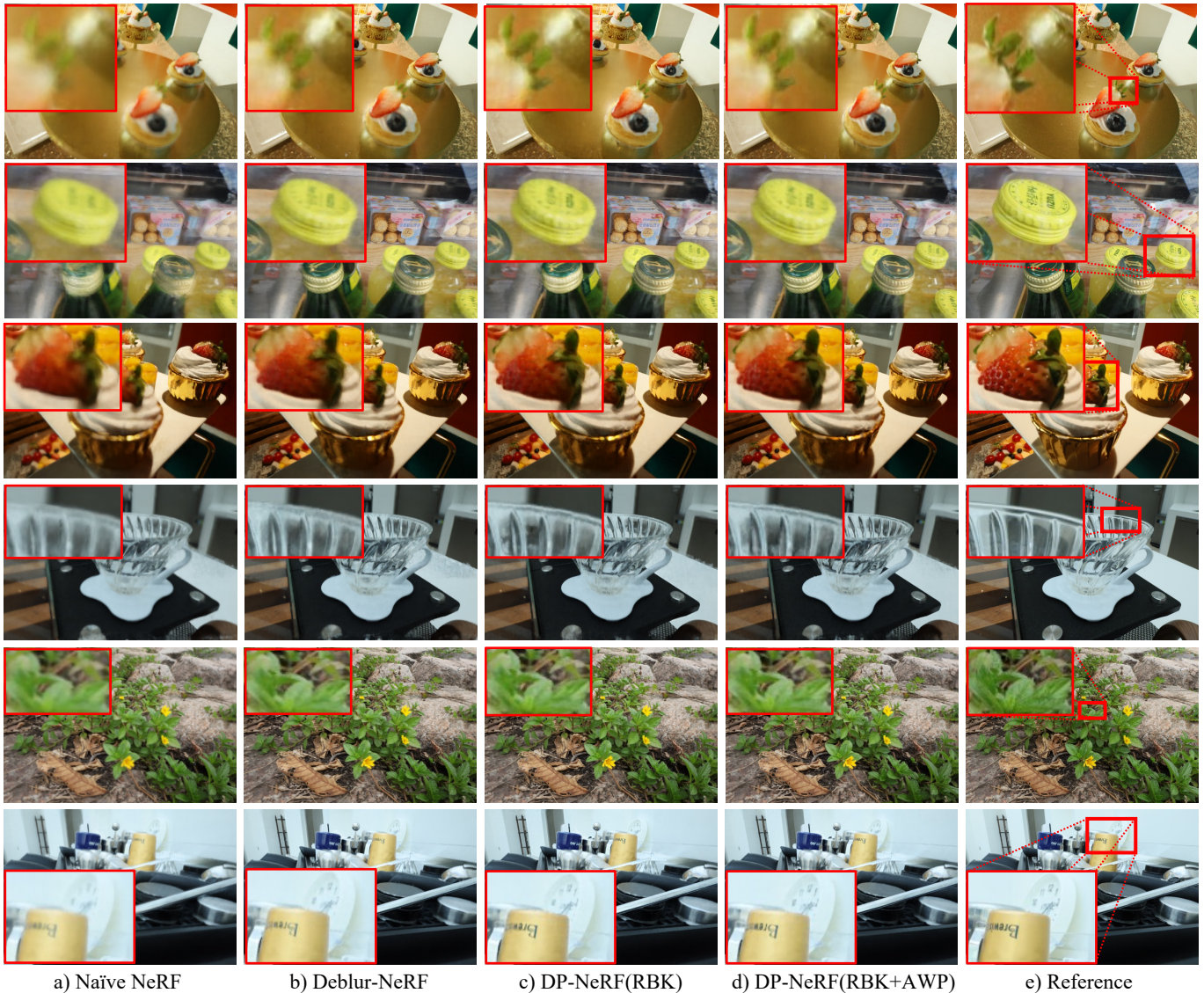


Figure 13. Rendered novel view synthesis results of DP-NeRF for real scene defocus blur. Figures (a)-(e) denote Naive NeRF, Deblur-NeRF, ours(RBK), ours(RBK+AWP), and ground truth images, respectively. Red colored box in corner of images are enlarged part of same colored box region in reference images.

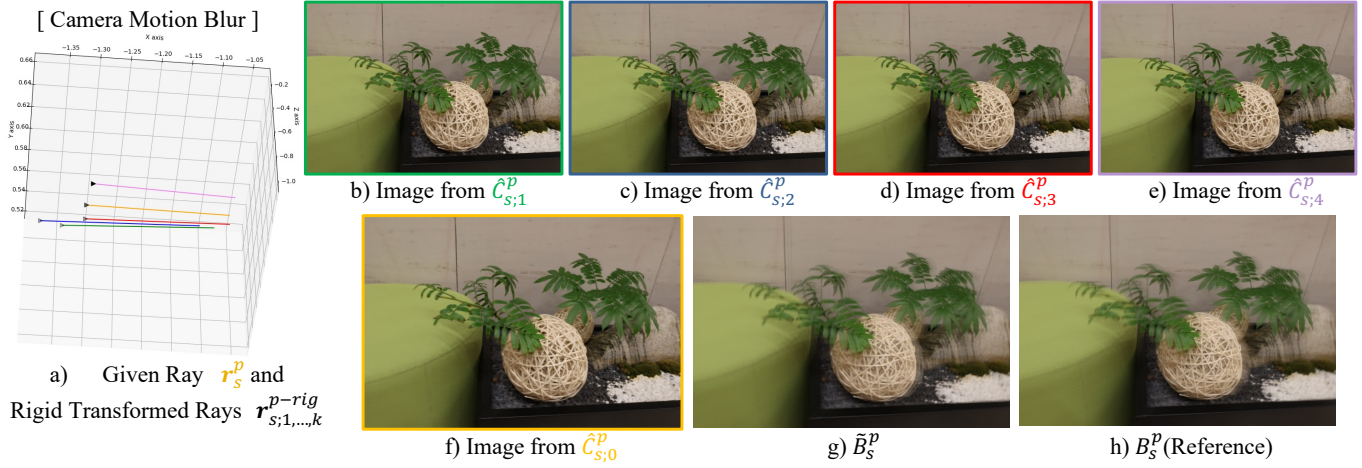


Figure 14. RBK analysis on camera motion blur for real **blurball** scene. Figure (a) denotes visualization result of original and rigid transformed camera origin and direction on given reference view, which is presented in Figure (h). Figures (b)-(f) denote rendered images from given and transformed cameras in Figure (a). Figure (g) denotes a composited blurred image from Figures (b)-to-(f) with composition weights to predict a reference image, Figure (h). Figures (g) and (h) are used in DP-NeRF as RGB reconstruction loss.

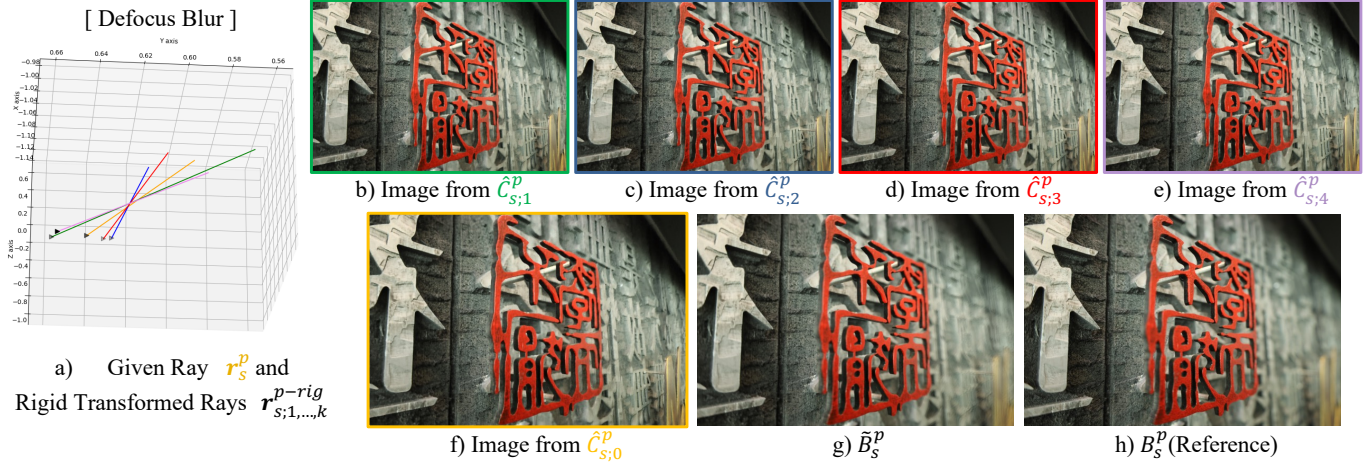


Figure 15. RBK analysis on defocus blur for real **defocuseal** scene. Figure (a) denotes visualization result of original and rigid transformed camera origin and direction on given reference view, which is presented in Figure (h). Figures (b)-(f) denote rendered images from camera and transformed cameras in Figure (a). Figure (g) denotes a composited blurred image from Figures (b)-(f) with composition weights to predict a reference image, Figure (h). Figure (g) and (h) are used in DP-NeRF as RGB reconstruction loss.

Camera Motion	Factory			Cozyroom			Pool			Tanabata			Trolley			Average		
	PSNR(↑)	SSIM(↑)	LPIPS(↓)	PSNR(↑)	SSIM(↑)	LPIPS(↓)	PSNR(↑)	SSIM(↑)	LPIPS(↓)	PSNR(↑)	SSIM(↑)	LPIPS(↓)	PSNR(↑)	SSIM(↑)	LPIPS(↓)	PSNR(↑)	SSIM(↑)	LPIPS(↓)
Naive NeRF [26]	19.32	.4563	.5304	25.66	.7941	.2288	30.45	.8354	.1932	22.22	.6807	.3653	21.25	.6370	.3633	23.78	.6807	.3362
DP-NeRF(RBK)	25.82	.7853	.2493	32.75	.9331	.0351	31.98	.8756	.0925	27.63	.8745	.1045	27.93	.8723	.1130	29.22	.8682	.1189
DP-NeRF(RBK+AWP)	25.91	.7787	.2494	32.65	.9317	.0355	31.96	.8768	.0908	27.61	.8748	.1033	28.03	.8752	.1129	29.23	.8674	.1184

Defocus	Factory			Cozyroom			Pool			Tanabata			Trolley			Average		
	PSNR(↑)	SSIM(↑)	LPIPS(↓)	PSNR(↑)	SSIM(↑)	LPIPS(↓)	PSNR(↑)	SSIM(↑)	LPIPS(↓)	PSNR(↑)	SSIM(↑)	LPIPS(↓)	PSNR(↑)	SSIM(↑)	LPIPS(↓)	PSNR(↑)	SSIM(↑)	LPIPS(↓)
Naive NeRF [26]	25.36	.7847	.2351	30.03	.8926	.0885	27.77	.7266	.3340	23.80	.7811	.2142	22.67	.7103	.2799	25.93	.7791	.2303
DP-NeRF(RBK)	28.56	.8672	.1052	32.00	.9207	.0410	31.18	.8482	.1577	26.51	.8586	.0802	26.00	.8277	.1200	28.85	.8645	.1008
DP-NeRF(RBK+AWP)	29.26	.8793	.1035	32.11	.9215	.0386	31.44	.8529	.1563	27.05	.8635	.0779	26.79	.8395	.1170	29.33	.8713	.0987

Table 6. Ablation study for the synthetic scene. Each color shading indicates the best and second-best result, respectively.

Camera Motion	Ball			Basket			Buick			Coffee			Decoration		
	PSNR(↑)	SSIM(↑)	LPIPS(↓)	PSNR(↑)	SSIM(↑)	LPIPS(↓)	PSNR(↑)	SSIM(↑)	LPIPS(↓)	PSNR(↑)	SSIM(↑)	LPIPS(↓)	PSNR(↑)	SSIM(↑)	LPIPS(↓)
Naive NeRF [26]	24.08	.6237	.3992	23.72	.7086	.3223	21.59	.6325	.3502	26.48	.8064	.2896	22.39	.6609	.3633
DP-NeRF(RBK)	27.15	.7641	.2112	27.35	.8367	.1347	24.93	.7791	.1545	30.72	.8949	.1070	24.15	.7730	.1700
DP-NeRF(RBK+AWP)	27.20	.7652	.2088	27.74	.8455	.1294	25.70	.7922	.1405	31.19	.9049	.1002	24.31	.7811	.1639

Camera motion	Girl			Heron			Parterre			Puppet			Stair			Average		
	PSNR(↑)	SSIM(↑)	LPIPS(↓)	PSNR(↑)	SSIM(↑)	LPIPS(↓)	PSNR(↑)	SSIM(↑)	LPIPS(↓)	PSNR(↑)	SSIM(↑)	LPIPS(↓)	PSNR(↑)	SSIM(↑)	LPIPS(↓)	PSNR(↑)	SSIM(↑)	LPIPS(↓)
Naive NeRF [26]	20.07	.7075	.3196	20.50	.5217	.4129	23.14	.6201	.4046	22.09	.6093	.3389	22.87	.4561	.4868	22.69	.6347	.3687
DP-NeRF(RBK)	22.19	.7934	.1575	22.55	.6831	.1970	25.81	.7635	.1931	25.19	.7497	.1493	25.68	.6446	.1799	25.57	.7682	.1654
DP-NeRF(RBK+AWP)	23.33	.8139	.1498	22.88	.6930	.1914	25.86	.7665	.1900	25.25	.7536	.1505	25.59	.6349	.1772	25.91	.7751	.1602

Table 7. Ablation study for the real scene camera motion blur. Each color shading indicates the best and second-best result, respectively.

Defocus	Cake			Caps			Cisco			Cupcake			Coral		
	PSNR(↑)	SSIM(↑)	LPIPS(↓)	PSNR(↑)	SSIM(↑)	LPIPS(↓)	PSNR(↑)	SSIM(↑)	LPIPS(↓)	PSNR(↑)	SSIM(↑)	LPIPS(↓)	PSNR(↑)	SSIM(↑)	LPIPS(↓)
Naive NeRF [26]	24.42	.7210	.2250	22.73	.6312	.2801	20.72	.7217	.1256	21.88	.6809	.2155	19.81	.5658	.2689
DP-NeRF(RBK)	25.80	.7704	.1251	23.72	.7003	.1486	20.68	.7232	.0889	22.51	.7331	.1003	20.02	.6052	.1183
DP-NeRF(RBK+AWP)	26.16	.7781	.1267	23.95	.7122	.1430	20.73	.7260	.0840	22.80	.7409	.0960	20.11	.6107	.1178

Defocus	Cups			Daisy			Sausage			Seal			Tools			Average		
	PSNR(↑)	SSIM(↑)	LPIPS(↓)	PSNR(↑)	SSIM(↑)	LPIPS(↓)	PSNR(↑)	SSIM(↑)	LPIPS(↓)	PSNR(↑)	SSIM(↑)	LPIPS(↓)	PSNR(↑)	SSIM(↑)	LPIPS(↓)	PSNR(↑)	SSIM(↑)	LPIPS(↓)
Naive NeRF [26]	25.02	.7581	.2315	22.74	.6203	.2621	17.79	.4830	.2789	22.79	.6267	.2680	26.08	.8523	.1547	22.40	.6661	.2310
DP-NeRF(RBK)	26.59	.8086	.1077	23.77	.6968	.1059	18.40	.5448	.1452	26.04	.7767	.0996	27.87	.8947	.0540	23.54	.7254	.1093
DP-NeRF(RBK+AWP)	26.75	.8136	.1035	23.79	.6971	.1075	18.35	.5443	.1473	25.95	.7779	.1026	28.07	.8980	.0539	23.67	.7299	.1082

Table 8. Ablation study for the real scene defocus blur. Each color shading indicates the best and second-best result, respectively.

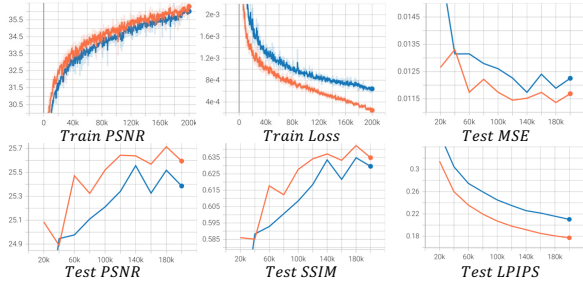


Figure 16. Training of DP-NeRF and Deblur-NeRF on *Stair* scene.

Model	PSNR(\uparrow)	SSIM(\uparrow)	LPIPS(\downarrow)
DP-NeRF(RBK)	24.93	.7791	.1545
DP-NeRF(RBK+AWP)	25.47	.7883	.1466
DP-NeRF(RBK+AWP+Coarse-to-Fine)	25.70	.7922	.1405

Table 9. Ablation of coarse-to-fine optimization on *Buick* scene.

C.3. Ablation of Coarse to Fine Optimization

We present the optimization graph for Deblur-NeRF [22] and DP-NeRF in Figure 16. Though it seems to be harder to optimize the DP-NeRF due to higher degree of freedom, DP-NeRF converges more faster than Deblur-NeRF thanks to the shared rigid motions in a single view, which works as regularization to optimize the RBK. In addition, we attach ablation results of the coarse-to-fine optimization in Table 9. It reveals that the proposed optimization scheme helps the model to take the full advantage of AWP and improves the visual quality. The time required to train 200000 iterations are around **9.5 hours** for Deblur-NeRF and **19 hours** for DP-NeRF on *two NVIDIA RTX 3090 GPU*s. Note that, we present representative scenes for Figure 16 and Table 9 due to time limitation to experiment on all scenes.

C.4. Ablation of the Number of Rigid Motions

We present the quantitative and qualitative results for the ablation analysis of the number of rigid motions in Table 10 and Figures 17 and 18. As we mentioned, LPIPS represents perceptual quality better than PSNR and SSIM do. Based on this metric, the perceptual quality of DP-NeRF gradually improves as the number of rigid motions increases. In addition, DP-NeRF exhibits higher perceptual quality than Deblur-NeRF [22] in terms of LPIPS for the same number of composition rays. Furthermore, RBK+AWP produces a better performance than does the RBK alone.

C.5. Visualization of Rigid Transformed Rays

We present additional visualization of rigid transformed rays predicted by the RBK for a specific view. Figure 19 and 20 show the transformed rays according to the change of the number of rigid motions k for camera motion and defocus blur, respectively. The rays colored as orange are original

center rays in all visualization, which are forwarded to RBK to generate the other rigidly warped rays in both Figure 19 and 20. They demonstrate that RBK successfully model the camera shaking and virtual aperture for camera motion and defocus blur, respectively.

C.6. Additional Error Map Visualization

As mentioned in the main paper, we present a full error map visualization without the emphasis box in Figure 21. Note that, brighter colors indicate greater error. We control the brightness and contrast in all output identically, to reveal the error between the models more prominently. Our model produces less error than the baselines for the images regardless of the blur type.

D. Supplementary Video

We attach videos outlining novel view synthesis. These videos are generated with spiral-path camera poses, which are widely used for visual comparison in NeRF-based research. Please watch these supplementary videos or visit our project page to observe the qualitative effectiveness of DP-NeRF.

# of RM	Camera Motion - Pool										Defocus - Pool							
	Deblur-NeRF			DP-NeRF(RBK)			DP-NeRF(RBK+AWP)				Deblur-NeRF			DP-NeRF(RBK)			DP-NeRF(RBK+AWP)	
	PSNR(\uparrow)	SSIM(\uparrow)	LPIPS(\downarrow)	PSNR(\uparrow)	SSIM(\uparrow)	LPIPS(\downarrow)	PSNR(\uparrow)	SSIM(\uparrow)	LPIPS(\downarrow)	PSNR(\uparrow)	SSIM(\uparrow)	LPIPS(\downarrow)	PSNR(\uparrow)	SSIM(\uparrow)	LPIPS(\downarrow)	PSNR(\uparrow)	SSIM(\uparrow)	LPIPS(\downarrow)
2	31.48	.8658	.1348	31.97	.8741	.1102	32.30	.8822	.1031	29.89	.8087	.2280	30.24	.8246	.2023	30.52	.8301	.1971
3	31.52	.8670	.1289	31.61	.8682	.1032	31.80	.8709	.0966	30.07	.8117	.2094	29.22	.7923	.1891	29.39	.8006	.1871
4	31.49	.8672	.1257	31.98	.8756	.0925	31.96	.8768	.0908	30.43	.8230	.1931	31.18	.8482	.1577	31.44	.8529	.1563
5	31.59	.8710	.1169	31.40	.8671	.0912	31.88	.8763	.0849	30.52	.8244	.1832	30.99	.8421	.1485	31.07	.8473	.1484
6	31.59	.8688	.1149	31.43	.8662	.0868	31.74	.8733	.0807	30.70	.8310	.1712	31.42	.8549	.1368	31.73	.8621	.1362
7	31.42	.8628	.1121	31.65	.8699	.0851	31.67	.8714	.0806	30.73	.8317	.1728	31.15	.8484	.1328	31.62	.8589	.1302
8	31.56	.8685	.1097	31.49	.8683	.0840	31.49	.8668	.0796	30.92	.8352	.1625	31.37	.8532	.1267	31.77	.8609	.1234

Table 10. Quantitative results for ablation study of the number of rigid motions in the main paper, which is denoted as RM in the table. Each color shading indicates **best** and **second-best** result on each scene with each model, respectively. Note that, the number of kernel points in Deblur-NeRF is set to (the number of rigid motions + 1) for fair comparison, which means the same number of composition rays to create a blurred color for a pixel.

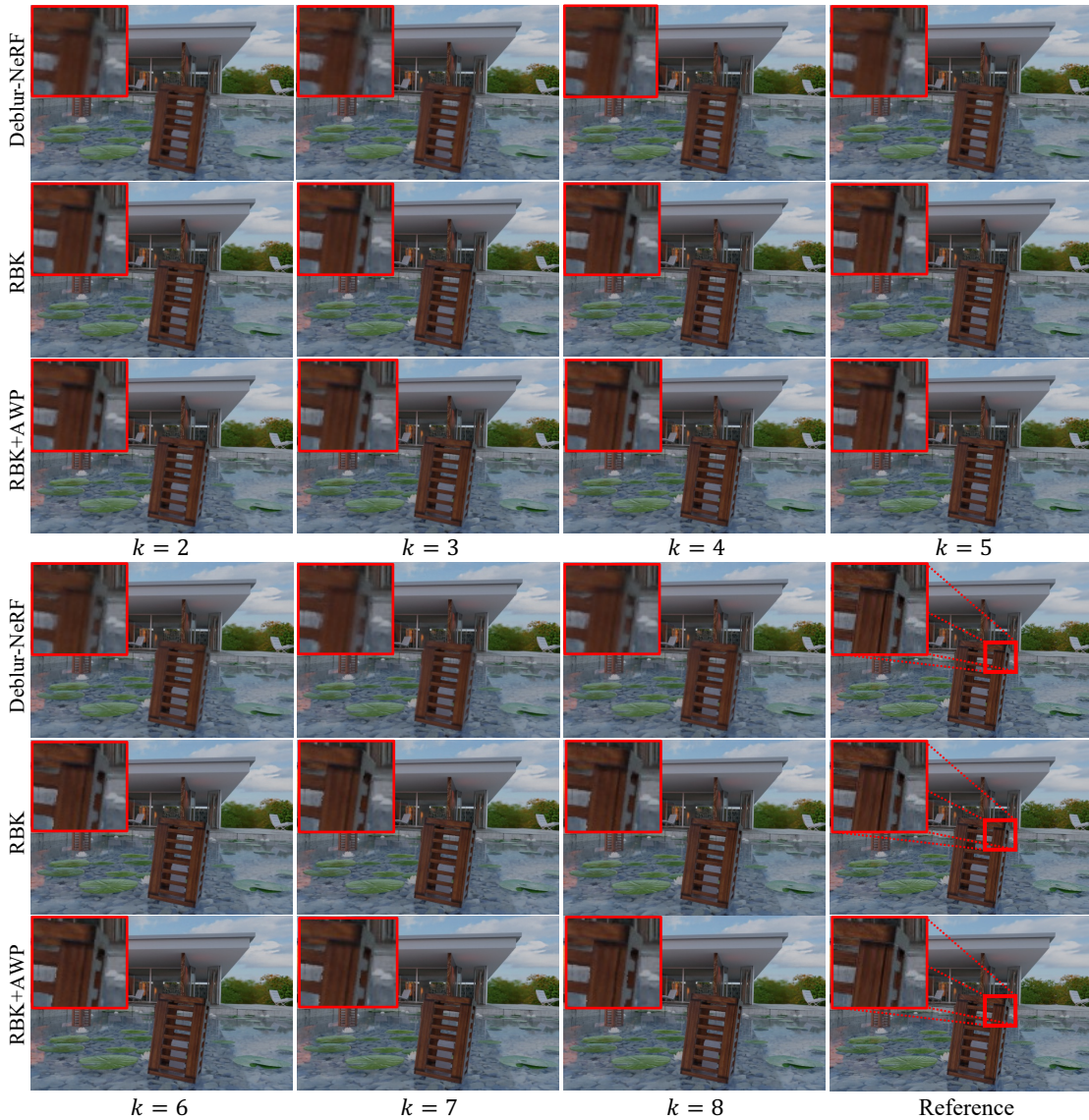


Figure 17. Qualitative results of ablation study depending on the number of rigid motion on camera motion blur scene. k denotes the number of rigid motion. Each row denotes Deblur-NeRF, DP-NeRF(RBK) and DP-NeRF(RBK+AWP), respectively. Red colored box in corner of images are enlarged part of same colored box region in reference images.



Figure 18. Qualitative results of ablation study depending on the number of rigid motion on defocus blur scene. k denotes the number of rigid motion. Each row denotes Deblur-NeRF, DP-NeRF(RBK) and DP-NeRF(RBK+AWP), respectively. Red colored box in corner of images are enlarged part of same colored box region in reference images.

[Camera Motion Blur]

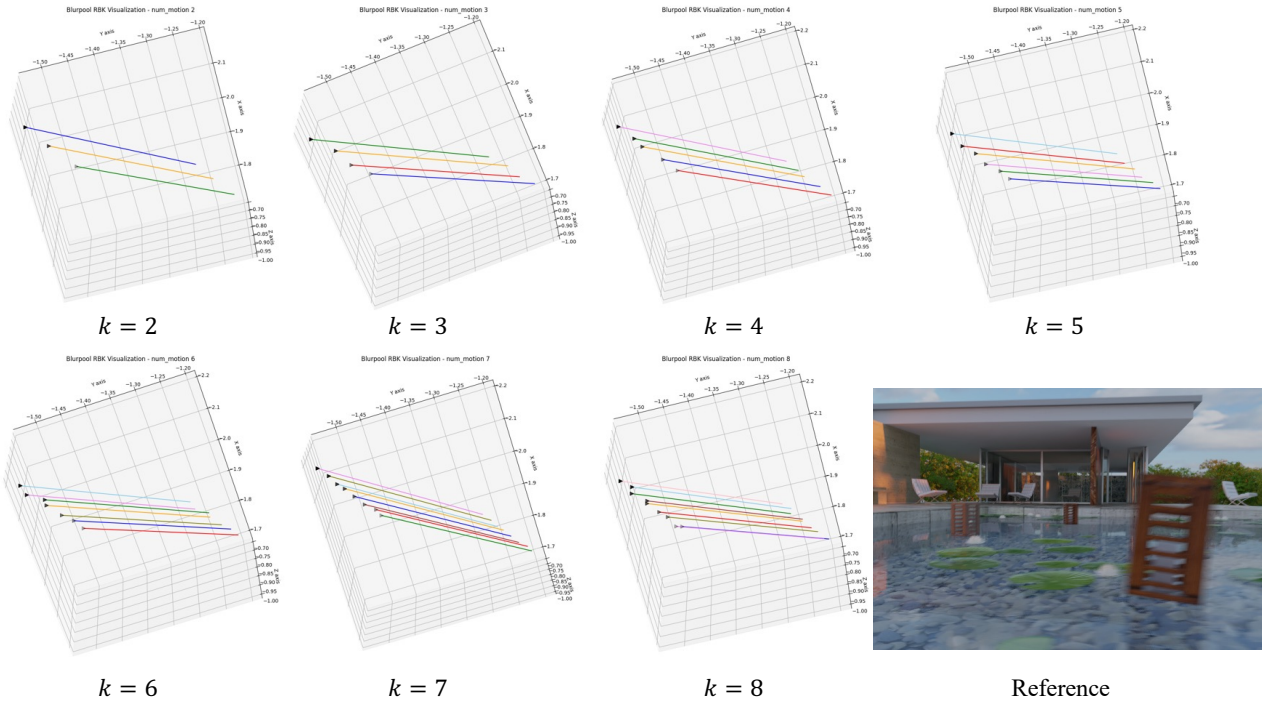


Figure 19. Visualization of warped poses using rigid motions predicted by the RBK according to the change of the number of rigid motion k on camera motion blur.

[Defocus Blur]

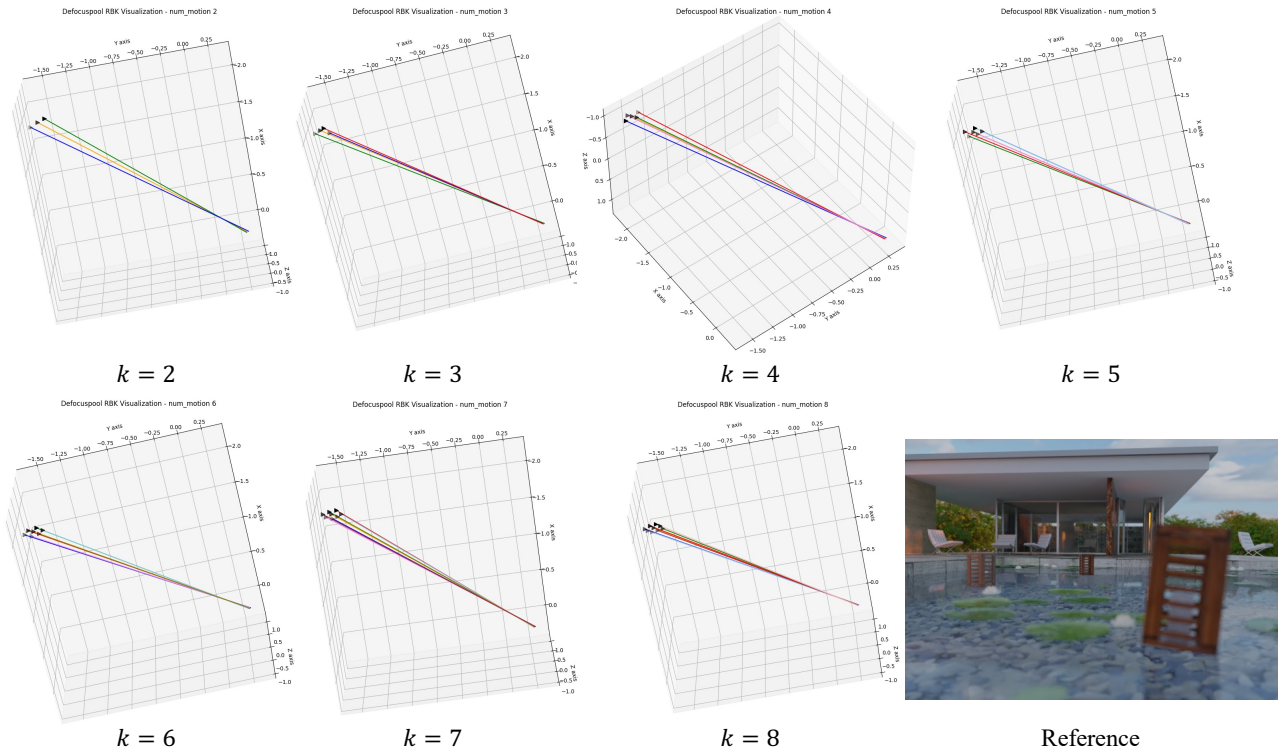


Figure 20. Visualization of warped poses using rigid motions predicted by the RBK according to the change of the number of rigid motion k on defocus blur.



Figure 21. Full error map visualization on defocus **Factory** and camera motion **Trolley** scene. In addition, we denote quantitative quality between reference and rendered images as average MSE(Mean Squared Error), denoted as **green text** on left bottom of each images.

References

- [1] Jonathan T Barron, Ben Mildenhall, Matthew Tancik, Peter Hedman, Ricardo Martin-Brualla, and Pratul P Srinivasan. Mip-nerf: A multiscale representation for anti-aliasing neural radiance fields. In *Proceedings of the IEEE/CVF International Conference on Computer Vision*, pages 5855–5864, 2021. 1, 2
- [2] Jonathan T Barron, Ben Mildenhall, Dor Verbin, Pratul P Srinivasan, and Peter Hedman. Mip-nerf 360: Unbounded anti-aliased neural radiance fields. In *Proceedings of the IEEE/CVF Conference on Computer Vision and Pattern Recognition*, pages 5470–5479, 2022. 1, 2
- [3] Sai Bi, Zexiang Xu, Pratul Srinivasan, Ben Mildenhall, Kalyan Sunkavalli, Miloš Hašan, Yannick Hold-Geoffroy, David Kriegman, and Ravi Ramamoorthi. Neural reflectance fields for appearance acquisition. *arXiv preprint arXiv:2008.03824*, 2020. 2
- [4] Piotr Bojanowski, Armand Joulin, David Lopez-Paz, and Arthur Szlam. Optimizing the latent space of generative networks. *arXiv preprint arXiv:1707.05776*, 2017. 4
- [5] Xiaogang Chen, Feng Li, Jie Yang, and Jingyi Yu. A theoretical analysis of camera response functions in image deblurring. In *European Conference on Computer Vision*, pages 333–346. Springer, 2012. 6
- [6] Xingyu Chen, Qi Zhang, Xiaoyu Li, Yue Chen, Ying Feng, Xuan Wang, and Jue Wang. Hallucinated neural radiance fields in the wild. In *Proceedings of the IEEE/CVF Conference on Computer Vision and Pattern Recognition*, pages 12943–12952, 2022. 1
- [7] Qingyong Hu, Bo Yang, Linhai Xie, Stefano Rosa, Yulan Guo, Zhihua Wang, Niki Trigoni, and Andrew Markham. Randa-net: Efficient semantic segmentation of large-scale point clouds. In *Proceedings of the IEEE/CVF Conference on Computer Vision and Pattern Recognition*, pages 11108–11117, 2020. 5, 9
- [8] Xin Huang, Qi Zhang, Ying Feng, Hongdong Li, Xuan Wang, and Qing Wang. Hdr-nerf: High dynamic range neural radiance fields. In *Proceedings of the IEEE/CVF Conference on Computer Vision and Pattern Recognition*, pages 18398–18408, 2022. 1, 2
- [9] Jiaya Jia. Single image motion deblurring using transparency. In *2007 IEEE Conference on computer vision and pattern recognition*, pages 1–8. IEEE, 2007. 3
- [10] Neel Joshi, C Lawrence Zitnick, Richard Szeliski, and David J Kriegman. Image deblurring and denoising using color priors. In *2009 IEEE Conference on Computer Vision and Pattern Recognition*, pages 1550–1557. IEEE, 2009. 3
- [11] Kim Jun-Seong, Kim Yu-Ji, Moon Ye-Bin, and Tae-Hyun Oh. Hdr-plenoxels: Self-calibrating high dynamic range radiance fields. *arXiv preprint arXiv:2208.06787*, 2022. 1, 2, 3
- [12] James T Kajiya and Brian P Von Herzen. Ray tracing volume densities. *ACM SIGGRAPH computer graphics*, 18(3):165–174, 1984. 3
- [13] Diederik P Kingma and Jimmy Ba. Adam: A method for stochastic optimization. *arXiv preprint arXiv:1412.6980*, 2014. 6
- [14] Dilip Krishnan, Terence Tay, and Rob Fergus. Blind deconvolution using a normalized sparsity measure. In *CVPR 2011*, pages 233–240. IEEE, 2011. 3
- [15] Orest Kupyn, Volodymyr Budzan, Mykola Mykhailych, Dmytro Mishkin, and Jiří Matas. Deblurgan: Blind motion deblurring using conditional adversarial networks. In *Proceedings of the IEEE conference on computer vision and pattern recognition*, pages 8183–8192, 2018. 3
- [16] Orest Kupyn, Tetiana Martyniuk, Junru Wu, and Zhangyang Wang. Deblurgan-v2: Deblurring (orders-of-magnitude) faster and better. In *Proceedings of the IEEE/CVF International Conference on Computer Vision*, pages 8878–8887, 2019. 3
- [17] Tianye Li, Mira Slavcheva, Michael Zollhoefer, Simon Green, Christoph Lassner, Changil Kim, Tanner Schmidt, Steven Lovegrove, Michael Goesele, Richard Newcombe, et al. Neural 3d video synthesis from multi-view video. In *Proceedings of the IEEE/CVF Conference on Computer Vision and Pattern Recognition*, pages 5521–5531, 2022. 1, 2
- [18] Zhengqi Li, Simon Niklaus, Noah Snavely, and Oliver Wang. Neural scene flow fields for space-time view synthesis of dynamic scenes. In *Proceedings of the IEEE/CVF Conference on Computer Vision and Pattern Recognition*, pages 6498–6508, 2021. 1, 2, 8
- [19] Stephen Lombardi, Tomas Simon, Jason Saragih, Gabriel Schwartz, Andreas Lehrmann, and Yaser Sheikh. Neural volumes: Learning dynamic renderable volumes from images. *arXiv preprint arXiv:1906.07751*, 2019. 1, 2
- [20] Leon B Lucy. An iterative technique for the rectification of observed distributions. *The astronomical journal*, 79:745, 1974. 3
- [21] Kevin M Lynch and Frank C Park. *Modern robotics*. Cambridge University Press, 2017. 4
- [22] Li Ma, Xiaoyu Li, Jing Liao, Qi Zhang, Xuan Wang, Jue Wang, and Pedro V Sander. Deblur-nerf: Neural radiance fields from blurry images. In *Proceedings of the IEEE/CVF Conference on Computer Vision and Pattern Recognition*, pages 12861–12870, 2022. 1, 2, 3, 4, 6, 7, 8, 9, 10, 11, 12, 13, 16
- [23] Ricardo Martin-Brualla, Noha Radwan, Mehdi SM Sajjadi, Jonathan T Barron, Alexey Dosovitskiy, and Daniel Duckworth. Nerf in the wild: Neural radiance fields for unconstrained photo collections. In *Proceedings of the IEEE/CVF Conference on Computer Vision and Pattern Recognition*, pages 7210–7219, 2021. 1, 2
- [24] Nelson Max. Optical models for direct volume rendering. *IEEE Transactions on Visualization and Computer Graphics*, 1(2):99–108, 1995. 3
- [25] Ben Mildenhall, Peter Hedman, Ricardo Martin-Brualla, Pratul P Srinivasan, and Jonathan T Barron. Nerf in the dark: High dynamic range view synthesis from noisy raw images. In *Proceedings of the IEEE/CVF Conference on Computer Vision and Pattern Recognition*, pages 16190–16199, 2022. 1, 2
- [26] Ben Mildenhall, Pratul P Srinivasan, Matthew Tancik, Jonathan T Barron, Ravi Ramamoorthi, and Ren Ng. Nerf:

- Representing scenes as neural radiance fields for view synthesis. In *Computer Vision–ECCV 2020: 16th European Conference, Glasgow, UK, August 23–28, 2020, Proceedings, Part I*, pages 405–421, 2020. 1, 3, 7, 9, 11, 12, 13, 15
- [27] Seungjun Nah, Tae Hyun Kim, and Kyoung Mu Lee. Deep multi-scale convolutional neural network for dynamic scene deblurring. In *Proceedings of the IEEE conference on computer vision and pattern recognition*, pages 3883–3891, 2017. 3
- [28] Michael Niemeyer and Andreas Geiger. Giraffe: Representing scenes as compositional generative neural feature fields. In *Proceedings of the IEEE/CVF Conference on Computer Vision and Pattern Recognition*, pages 11453–11464, 2021. 2
- [29] Keunhong Park, Utkarsh Sinha, Jonathan T Barron, Sofien Bouaziz, Dan B Goldman, Steven M Seitz, and Ricardo Martin-Brualla. Nerfies: Deformable neural radiance fields. In *Proceedings of the IEEE/CVF International Conference on Computer Vision*, pages 5865–5874, 2021. 1, 2, 4, 5, 7, 8, 10
- [30] Keunhong Park, Utkarsh Sinha, Peter Hedman, Jonathan T Barron, Sofien Bouaziz, Dan B Goldman, Ricardo Martin-Brualla, and Steven M Seitz. Hypernerf: A higher-dimensional representation for topologically varying neural radiance fields. *arXiv preprint arXiv:2106.13228*, 2021. 1, 2
- [31] Sida Peng, Junting Dong, Qianqian Wang, Shangzhan Zhang, Qing Shuai, Xiaowei Zhou, and Hujun Bao. Animatable neural radiance fields for modeling dynamic human bodies. In *Proceedings of the IEEE/CVF International Conference on Computer Vision*, pages 14314–14323, 2021. 2
- [32] Julien Philip, Sébastien Mordant, Michaël Gharbi, and George Drettakis. Free-viewpoint indoor neural relighting from multi-view stereo. *ACM Transactions on Graphics (TOG)*, 40(5):1–18, 2021. 2
- [33] Albert Pumarola, Enric Corona, Gerard Pons-Moll, and Francesc Moreno-Noguer. D-nerf: Neural radiance fields for dynamic scenes. In *Proceedings of the IEEE/CVF Conference on Computer Vision and Pattern Recognition*, pages 10318–10327, 2021. 1, 2, 8
- [34] William Hadley Richardson. Bayesian-based iterative method of image restoration. *JoSA*, 62(1):55–59, 1972. 3
- [35] Olinde Rodrigues. *De l’attraction des sphéroïdes, Correspondence sur l’École Impériale Polytechnique*. PhD thesis, PhD thesis, Thesis for the Faculty of Science of the University of Paris, 1816. 4
- [36] Johannes L Schonberger and Jan-Michael Frahm. Structure-from-motion revisited. In *Proceedings of the IEEE conference on computer vision and pattern recognition*, pages 4104–4113, 2016. 6
- [37] Johannes L Schönberger, Enliang Zheng, Jan-Michael Frahm, and Marc Pollefeys. Pixelwise view selection for unstructured multi-view stereo. In *European conference on computer vision*, pages 501–518. Springer, 2016. 6
- [38] Katja Schwarz, Yiyi Liao, Michael Niemeyer, and Andreas Geiger. Graf: Generative radiance fields for 3d-aware image synthesis. *Advances in Neural Information Processing Systems*, 33:20154–20166, 2020. 2
- [39] Qi Shan, Jiaya Jia, and Aseem Agarwala. High-quality motion deblurring from a single image. *Acm transactions on graphics (tog)*, 27(3):1–10, 2008. 3
- [40] Hyeongseok Son, Junyong Lee, Sunghyun Cho, and Seungyong Lee. Single image defocus deblurring using kernel-sharing parallel atrous convolutions. In *Proceedings of the IEEE/CVF International Conference on Computer Vision*, pages 2642–2650, 2021. 6, 7
- [41] Hyeongseok Son, Junyong Lee, Jonghyeop Lee, Sunghyun Cho, and Seungyong Lee. Recurrent video deblurring with blur-invariant motion estimation and pixel volumes. *ACM Transactions on Graphics (TOG)*, 40(5):1–18, 2021. 6, 7
- [42] Pratul P Srinivasan, Boyang Deng, Xiuming Zhang, Matthew Tancik, Ben Mildenhall, and Jonathan T Barron. Nerv: Neural reflectance and visibility fields for relighting and view synthesis. In *Proceedings of the IEEE/CVF Conference on Computer Vision and Pattern Recognition*, pages 7495–7504, 2021. 2
- [43] Pratul P Srinivasan, Rahul Garg, Neal Wadhwa, Ren Ng, and Jonathan T Barron. Aperture supervision for monocular depth estimation. In *Proceedings of the IEEE Conference on Computer Vision and Pattern Recognition*, pages 6393–6401, 2018. 2, 5, 11
- [44] Pratul P Srinivasan, Ren Ng, and Ravi Ramamoorthi. Light field blind motion deblurring. In *Proceedings of the IEEE Conference on Computer Vision and Pattern Recognition*, pages 3958–3966, 2017. 2, 5, 11
- [45] Shih-Yang Su, Frank Yu, Michael Zollhöfer, and Helge Rhodin. A-nerf: Articulated neural radiance fields for learning human shape, appearance, and pose. *Advances in Neural Information Processing Systems*, 34:12278–12291, 2021. 2
- [46] Jian Sun, Wenfei Cao, Zongben Xu, and Jean Ponce. Learning a convolutional neural network for non-uniform motion blur removal. In *Proceedings of the IEEE conference on computer vision and pattern recognition*, pages 769–777, 2015. 3
- [47] Jiaming Sun, Yiming Xie, Linghao Chen, Xiaowei Zhou, and Hujun Bao. Neuralrecon: Real-time coherent 3d reconstruction from monocular video. In *Proceedings of the IEEE/CVF Conference on Computer Vision and Pattern Recognition*, pages 15598–15607, 2021. 2
- [48] Xin Tao, Hongyun Gao, Xiaoyong Shen, Jue Wang, and Jiaya Jia. Scale-recurrent network for deep image deblurring. In *Proceedings of the IEEE conference on computer vision and pattern recognition*, pages 8174–8182, 2018. 3
- [49] Edgar Tretschk, Ayush Tewari, Vladislav Golyanik, Michael Zollhöfer, Christoph Lassner, and Christian Theobalt. Non-rigid neural radiance fields: Reconstruction and novel view synthesis of a dynamic scene from monocular video. In *Proceedings of the IEEE/CVF International Conference on Computer Vision*, pages 12959–12970, 2021. 1, 2
- [50] Peng Wang, Lingjie Liu, Yuan Liu, Christian Theobalt, Taku Komura, and Wenping Wang. Neus: Learning neural implicit surfaces by volume rendering for multi-view reconstruction. *arXiv preprint arXiv:2106.10689*, 2021. 2
- [51] Tiange Xiang, Chaoyi Zhang, Yang Song, Jianhui Yu, and Weidong Cai. Walk in the cloud: Learning curves for point

- clouds shape analysis. In *Proceedings of the IEEE/CVF International Conference on Computer Vision*, pages 915–924, 2021. 5
- [52] Alex Yu, Sara Fridovich-Keil, Matthew Tancik, Qinhong Chen, Benjamin Recht, and Angjoo Kanazawa. Plenoxels: Radiance fields without neural networks. *arXiv preprint arXiv:2112.05131*, 2021. 3
- [53] Syed Waqas Zamir, Aditya Arora, Salman Khan, Munawar Hayat, Fahad Shahbaz Khan, Ming-Hsuan Yang, and Ling Shao. Multi-stage progressive image restoration. In *Proceedings of the IEEE/CVF conference on computer vision and pattern recognition*, pages 14821–14831, 2021. 3, 6, 7
- [54] Hongguang Zhang, Yuchao Dai, Hongdong Li, and Piotr Koniusz. Deep stacked hierarchical multi-patch network for image deblurring. In *Proceedings of the IEEE/CVF Conference on Computer Vision and Pattern Recognition*, pages 5978–5986, 2019. 3
- [55] Jiakai Zhang, Xinhang Liu, Xinyi Ye, Fuqiang Zhao, Yanshun Zhang, Minye Wu, Yingliang Zhang, Lan Xu, and Jingyi Yu. Editable free-viewpoint video using a layered neural representation. *ACM Transactions on Graphics (TOG)*, 40(4):1–18, 2021. 1, 2
- [56] Richard Zhang, Phillip Isola, Alexei A Efros, Eli Shechtman, and Oliver Wang. The unreasonable effectiveness of deep features as a perceptual metric. In *Proceedings of the IEEE conference on computer vision and pattern recognition*, pages 586–595, 2018. 6
- [57] Xiuming Zhang, Pratul P Srinivasan, Boyang Deng, Paul Debevec, William T Freeman, and Jonathan T Barron. Nerfactor: Neural factorization of shape and reflectance under an unknown illumination. *ACM Transactions on Graphics (TOG)*, 40(6):1–18, 2021. 1
- [58] Fuqiang Zhao, Wei Yang, Jiakai Zhang, Pei Lin, Yingliang Zhang, Jingyi Yu, and Lan Xu. Humannerf: Efficiently generated human radiance field from sparse inputs. In *Proceedings of the IEEE/CVF Conference on Computer Vision and Pattern Recognition*, pages 7743–7753, 2022. 2
- [59] Zelin Zhao and Jiaya Jia. End-to-end view synthesis via nerf attention. *arXiv preprint arXiv:2207.14741*, 2022. 2, 5, 9